Article

Developmental Cell

# Excess neuropeptides in lung signal through endothelial cells to impair gas exchange

## Graphical abstract

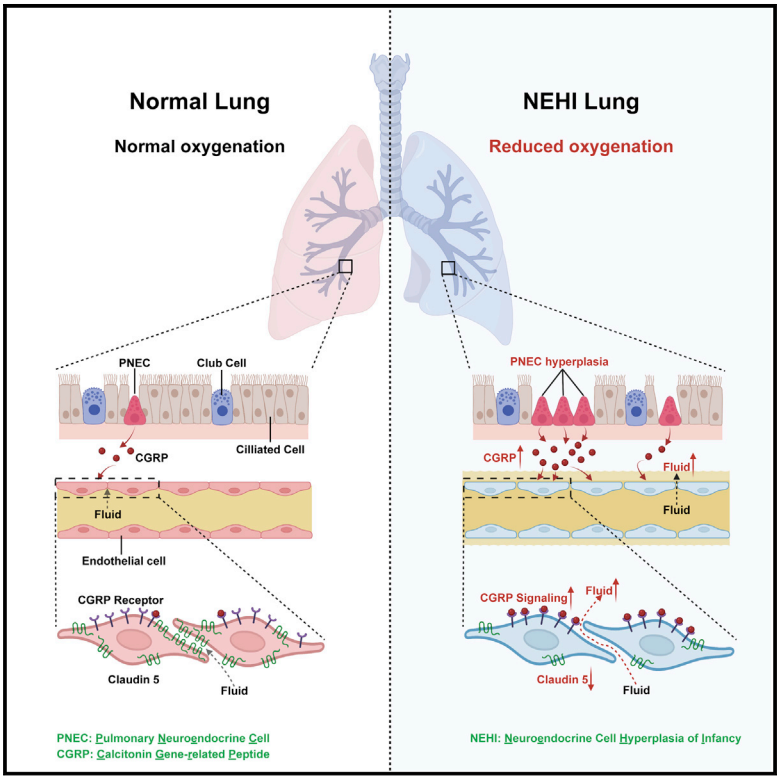


## Highlights

- Increased PNECs are responsible for poor gas exchange in a NEHI mouse model
- Increased PNECs and CGRP led to impaired endothelial barrier and excess fluid
- Antagonizing CGRP signaling improved barrier and oxygenation in NEHI mouse mutants
- Increased neuropeptides and reduced endothelial junctions were found in ARDS lungs

## Authors

Jinhao Xu, Le Xu, Pengfei Sui, ..., Gail Deutsch, Lisa R. Young, Xin Sun

## Correspondence

xinsun@health.ucsd.edu

## In brief

Xu et al. show that increased pulmonary neuroendocrine cells (PNECs), and secreted neuropeptides can cause poor gas exchange. In neuroendocrine hyperplasia of infancy (NEHI) mice, increased CGRP from PNECs causes vessel leakage, excess fluid, and poor oxygenation. These findings suggest neuropeptides as therapeutic targets for conditions with excess lung fluid.

Xu et al., 2022, Developmental Cell *57*, 1–15
April 11, 2022 
https://doi.org/10.1016/j.devcel.2022.02.023

CellPress

Please cite this article in press as: Xu et al., Excess neuropeptides in lung signal through endothelial cells to impair gas exchange, Developmental Cell (2022), https://doi.org/10.1016/j.devcel.2022.02.023

Developmental Cell

CellPress

Article

# Excess neuropeptides in lung signal through endothelial cells to impair gas exchange

Jinhao Xu,[1,2] Le Xu,[1] Pengfei Sui,[3] Jiyuan Chen,[4] Esteban A. Moya,[5] Patrick Hume,[6] William J. Janssen,[6] Jason M. Duran,[7] Patricia Thistlethwaite,[8] Aaron Carlin,[9] Peter Gulleman,[10] Brandon Banaschewski,[11] Mary Kate Goldy,[11] Jason X.-J. Yuan,[4] Atul Malhotra,[4] Gloria Pryhuber,[12] Laura Crotty-Alexander,[4,13] Gail Deutsch,[14] Lisa R. Young,[10,11] and Xin Sun[1,2,15,*]

[1]Department of Pediatrics, School of Medicine, University of California San Diego, La Jolla, CA 92093, USA
[2]Department of Biological Sciences, University of California San Diego, La Jolla, CA 92093, USA
[3]CAS Center for Excellence in Molecular Cell Science, Shanghai Institute of Biochemistry and Cell Biology, Chinese Academy of Sciences, 320 Yueyang Road, Shanghai 200031, China
[4]Division of Pulmonary, Critical Care and Sleep Medicine, School of Medicine, University of California San Diego, La Jolla, CA 92121, USA
[5]Division of Physiology, Department of Medicine, University of California San Diego, La Jolla, CA 92093, USA
[6]Department of Medicine, National Jewish Health, Denver, CO 80206, USA
[7]Division of Cardiology, Department of Internal Medicine, University of California San Diego Medical Center, La Jolla, CA 92037, USA
[8]Division of Cardiothoracic Surgery, University of California San Diego, La Jolla, CA 92093, USA
[9]Division of Infectious Diseases and Global Public Health, Department of Medicine, University of California San Diego, La Jolla, CA 92093, USA
[10]Department of Pediatrics, Vanderbilt University Medical Center, Nashville, TN 37232, USA
[11]Division of Pulmonary and Sleep Medicine, Department of Pediatrics, Children's Hospital of Philadelphia, Philadelphia, PA 16104, USA
[12]School of Medicine and Dentistry, University of Rochester Medical Center, Rochester, NY 14642, USA
[13]Veterans Affairs San Diego Healthcare System, La Jolla, CA 92161, USA
[14]Department of Laboratories, Seattle Children's Hospital, University of Washington, Seattle, WA 98105, USA
[15]Lead contact
*Correspondence: xinsun@health.ucsd.edu
https://doi.org/10.1016/j.devcel.2022.02.023

## SUMMARY

Although increased neuropeptides are often detected in lungs that exhibit respiratory distress, whether they contribute to the condition is unknown. Here, we show in a mouse model of neuroendocrine cell hyperplasia of infancy, a pediatric disease with increased pulmonary neuroendocrine cells (PNECs), excess PNEC-derived neuropeptides are responsible for pulmonary manifestations including hypoxemia. In mouse postnatal lung, prolonged signaling from elevated neuropeptides such as calcitonin gene-related peptide (CGRP) activate receptors enriched on endothelial cells, leading to reduced cellular junction gene expression, increased endothelium permeability, excess lung fluid, and hypoxemia. Excess fluid and hypoxemia were effectively attenuated by either prevention of PNEC formation, inactivation of CGRP gene, endothelium-specific inactivation of CGRP receptor gene, or treatment with CGRP receptor antagonist. Neuropeptides were increased in human lung diseases with excess fluid such as acute respiratory distress syndrome. Our findings suggest that restricting neuropeptide function may limit fluid and improve gas exchange in these conditions.

## INTRODUCTION

Efficient gas exchange requires matched conductance of air and blood to the ~480 million alveoli in lung (Ochs et al., 2004), with diffusion of oxygen and carbon dioxide across the alveolar epithelial and endothelial barriers. Disruption of barriers, such as in acute respiratory distress syndrome (ARDS) caused by lung injury or infection, leads to excess fluid in the interstitial and/or the alveolar space, impeding gas exchange and causing respiratory distress. Although multiple mechanisms contribute to ARDS, increases in select neuropeptides have been documented in the lungs of ARDS patients and in ARDS animal models (Espiritu et al., 1992). However, whether excess neuropeptides contribute to respiratory distress has not been addressed.

In the lung, a major cellular source of neuropeptides is pulmonary neuroendocrine cells (PNECs). PNECs represent a rare and evolutionarily conserved airway epithelial cell population (Xu et al., 2020). *In vitro*, these specialized cells respond to stimuli such as nicotine, hypoxia, and mechanical stretch by secreting potent bioactive neuropeptides and neurotransmitters (Cutz et al., 2007). *In vivo*, PNECs are activated following allergen

Please cite this article in press as: Xu et al., Excess neuropeptides in lung signal through endothelial cells to impair gas exchange, Developmental Cell (2022), https://doi.org/10.1016/j.devcel.2022.02.023



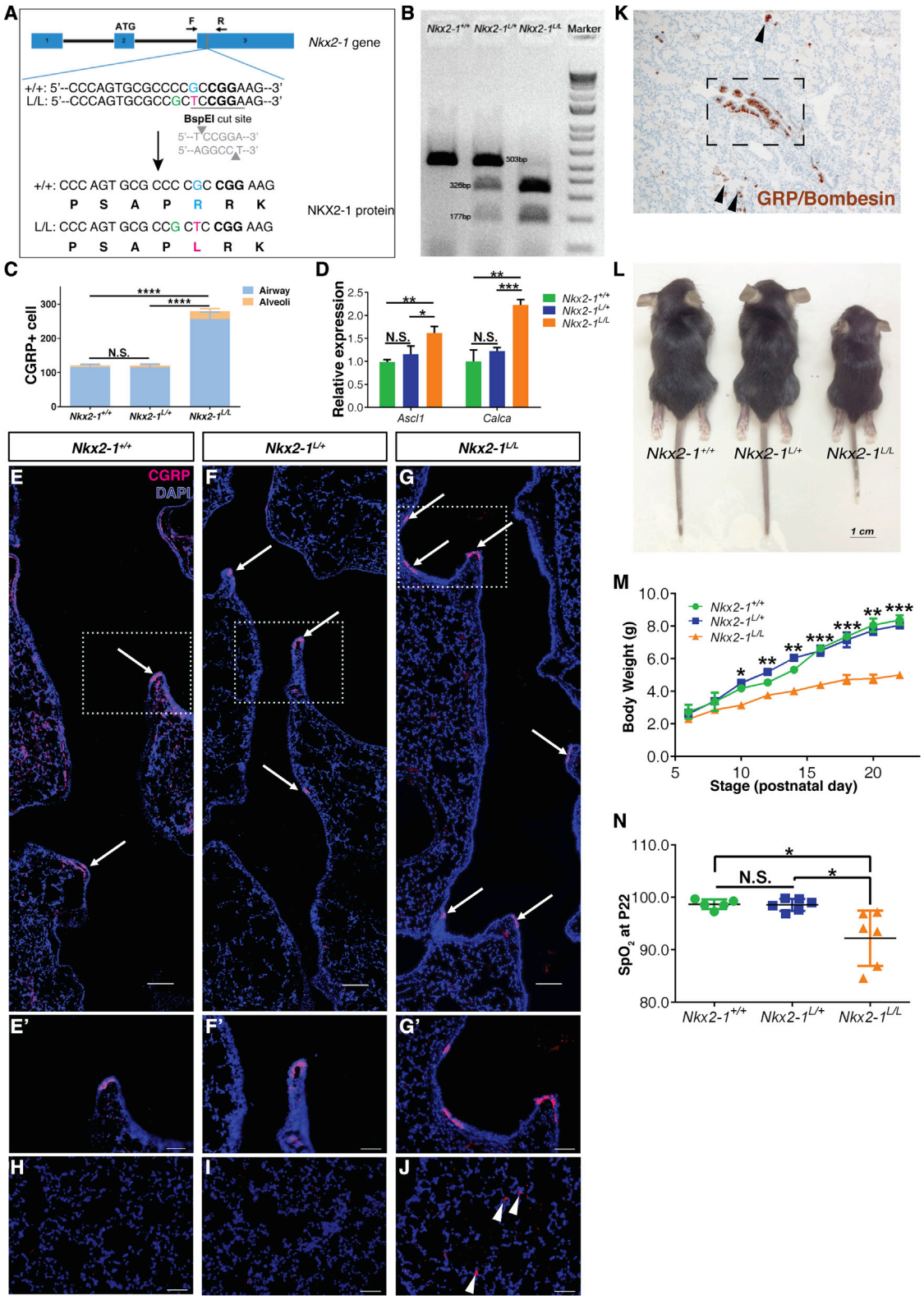


**Figure 1. Establishing the *Nkx2-1* mutant model of NEHI using CRISPR-Cas9 genome editing**

(A) Schematic of CRISPR-Cas9 strategy to generate *Nkx2-1*$^{R161L}$ (*Nkx2-1*$^{L}$) allele. Aside from engineered changes, a silent C → G change also arose in the CRISPR-Cas9 repair process and is noted in green.

(B) RFLP-based genotyping. Introduction of BspEI site in the mutant allele led to digestion of 503 bp PCR product into 326 bp and 177-bp fragments.

*(legend continued on next page)*

Please cite this article in press as: Xu et al., Excess neuropeptides in lung signal through endothelial cells to impair gas exchange, Developmental Cell (2022), https://doi.org/10.1016/j.devcel.2022.02.023



challenge and are essential for amplifying allergen-induced asthmatic responses (Sui et al., 2018). Increased PNECs have been recognized in a variety of lung diseases, including bronchopulmonary dysplasia (BPD), asthma, pulmonary hypertension, sudden infant death syndrome, and bronchiolitis obliterans (Cutz et al., 2007). However, it is debated whether the increase of this rare airway cell type is the cause or the consequence of poor gas exchange, and the repertoire and mechanisms governing PNEC function *in vivo* remains poorly understood.

Neuroendocrine cell hyperplasia of infancy (NEHI) is a rare childhood interstitial lung disease with unexplained and persistent respiratory symptoms (Deterding et al., 2005). Patients with NEHI are typically asymptomatic at birth but present with insidious onset of tachypnea, hypoxemia, crackles on chest auscultation, and failure to thrive in the first few months to years of age (Liptzin et al., 2020). A central puzzle with NEHI is the absence of alveolar simplification, a pathological feature that accompanies other conditions with gas exchange deficiency such as in chronic obstructive pulmonary disease (COPD) and BPD. In contrast to the lack of structural defect in the alveoli, the defining histological feature of NEHI is the characteristic PNEC hyperplasia as aggregates termed neuroendocrine epithelial bodies in the distal airways and alveolar ducts. However, it is debated whether the increase of a rare airway cell type would explain hypoxemia and respiratory symptoms. Most children with NEHI require supplemental oxygen for many years, as no disease-specific treatment for NEHI is currently available (Nevel et al., 2018).

In the present study, we established a mouse model of NEHI by generating mice that carry the first identified NEHI patient genetic variant, a point mutation in the transcription factor gene *NKX2-1* (Young et al., 2013). The mutant mice faithfully recapitulated key aspects of the clinical and pathologic phenotypes observed in children with NEHI. Through generation of multiple compound mutant, we demonstrated that increased PNECs and their associated neuropeptides are responsible for NEHI physiological phenotypes including reduced oxygenation. More importantly, mechanistic dissection revealed that excess PNEC production of neuropeptides such as calcitonin gene-related peptide (CGRP) signals through receptors on the endothelial cells to disrupt endothelial barrier, leading to excess fluid in lung. Treatment with a CGRP receptor antagonist reduced lung fluid and improved gas exchange in the NEHI model, raising the possibility that dampening excess neuropeptide signaling may help improve respiratory function.

## RESULTS

### *Nkx2-1*$^{R161L/R161L}$ mutants recapitulate key features of NEHI

To establish an animal model of NEHI, we used CRISPR-Cas9 technology to generate mice that carry an allele termed *Nkx2-1*$^{R161L}$, corresponding to the first patient mutation found in a family with NEHI (Figures 1A, 1B, and S1A) (Young et al., 2013). One round of CRISPR injection yielded 19 pups, 5 of which carried the intended change. To minimize effects of possible off-target mutation in any given founder, F1 progeny from different founders were bred to each other and phenotyping was carried out in their progeny.

To address if mice carrying the *Nkx2-1*$^{R161L}$ allele recapitulated NEHI phenotypes, we started with assessment of PNEC hyperplasia, the namesake feature of NEHI. By counting CGRP+ cells in whole lung lobes and assaying for transcript level of PNEC markers *Ascl1* and *Calca* (encoding CGRP), we found that *Nkx2-1*$^{R161L/R161L}$ mutants (hereafter referred to as *Nkx2-1*$^{L/L}$ mutants) exhibited increased numbers of PNECs compared with heterozygous (*Nkx2-1*$^{L/+}$) and wild-type (*Nkx2-1*$^{+/+}$) littermate controls (Figures 1C and 1D). A majority of the increased PNECs were found along the airway where PNECs are normally positioned (Figures 1E–1G). There was also a minor contribution (~6% of the total) from ectopic CGRP+ cells scattered in the alveolar region (Figures 1C and 1H–1J). In reviewing lung biopsies from patients with NEHI, we found evidence of a variable number of ectopic PNECs in the alveolar region, in addition to the documented increases in the airway (Figure 1K). The findings in NEHI mouse model were supported by costaining of another PNEC marker synaptophysin (SYP) together with CGRP (Figures S1B–S1B″). Quantification revealed that the CGRP+ PNEC proportion remained unchanged in *Nkx2-1*$^{L/L}$ mutants compared with other controls, further confirming PNEC number increase (Figure S1C).

In contrast to PNEC hyperplasia, the number and distribution of ciliated cells and club cells appeared normal in *Nkx2-1*$^{L/L}$ mutants compared with controls (Figures S1D–S1F and S1D′–S1F′). There was no ectopic presence of basal cells in the intrapulmonary airway of mouse mutants, similar to controls. Although goblet cells are present at baseline in normal human airways, their prominence has not been documented in NEHI. However, in contrast to the complete absence of goblet cells in mouse airway, in *Nkx2-1*$^{L/L}$ mutants, some distal airway cells coexpressed both the club cell marker SCGB1A1 and the goblet cell marker

(C) PNEC quantification of whole left lobe at E18.5 (n = 3 for each group), statistical analysis was performed on the total PNEC number (airway and alveoli combined).
(D) qPCR of PNEC markers *Ascl1* and *Calca* at P22 (n = 3 for each group).
(E–G) Representative longitudinal section of the main airway in P22 lung for each group with anti-CGRP staining labeling PNECs (arrows). Scale bars, 100 μm. (E′–G′) Magnified view of boxed areas in (E–G), respectively. Scale bars, 50 μm.
(H–J) CGRP+ cells (arrowheads) were ectopically detected in the alveolar region of *Nkx2-1*$^{L/L}$ mutants. Scale bars, 50 μm.
(K) NEHI patient biopsy with anti-GRP/Bombesin labeling of PNECs showing large neuroepithelial bodies (NEBs) at bronchiole (dashed box) and ectopic solitary PNECs in alveolar region (arrowheads).
(L) Representative body size at P22.
(M) Growth curve from P5 to P22 of 12 pups nursed by the same outbred foster mother (n = 4 for each group). Statistical analysis was carried out separately at each time point.
(N) Oxygen saturation at P22 (n ≥ 6 for each group).
One-way ANOVA Tukey's multiple comparisons test was used for (C, D, M, and N). N.S., not significant, $p \geq 0.05$. * for $p < 0.05$, ** for $p < 0.01$, *** for $p < 0.001$. Error bars represent mean ± SD.
See also Figure S1.

Please cite this article in press as: Xu et al., Excess neuropeptides in lung signal through endothelial cells to impair gas exchange, Developmental Cell (2022), https://doi.org/10.1016/j.devcel.2022.02.023



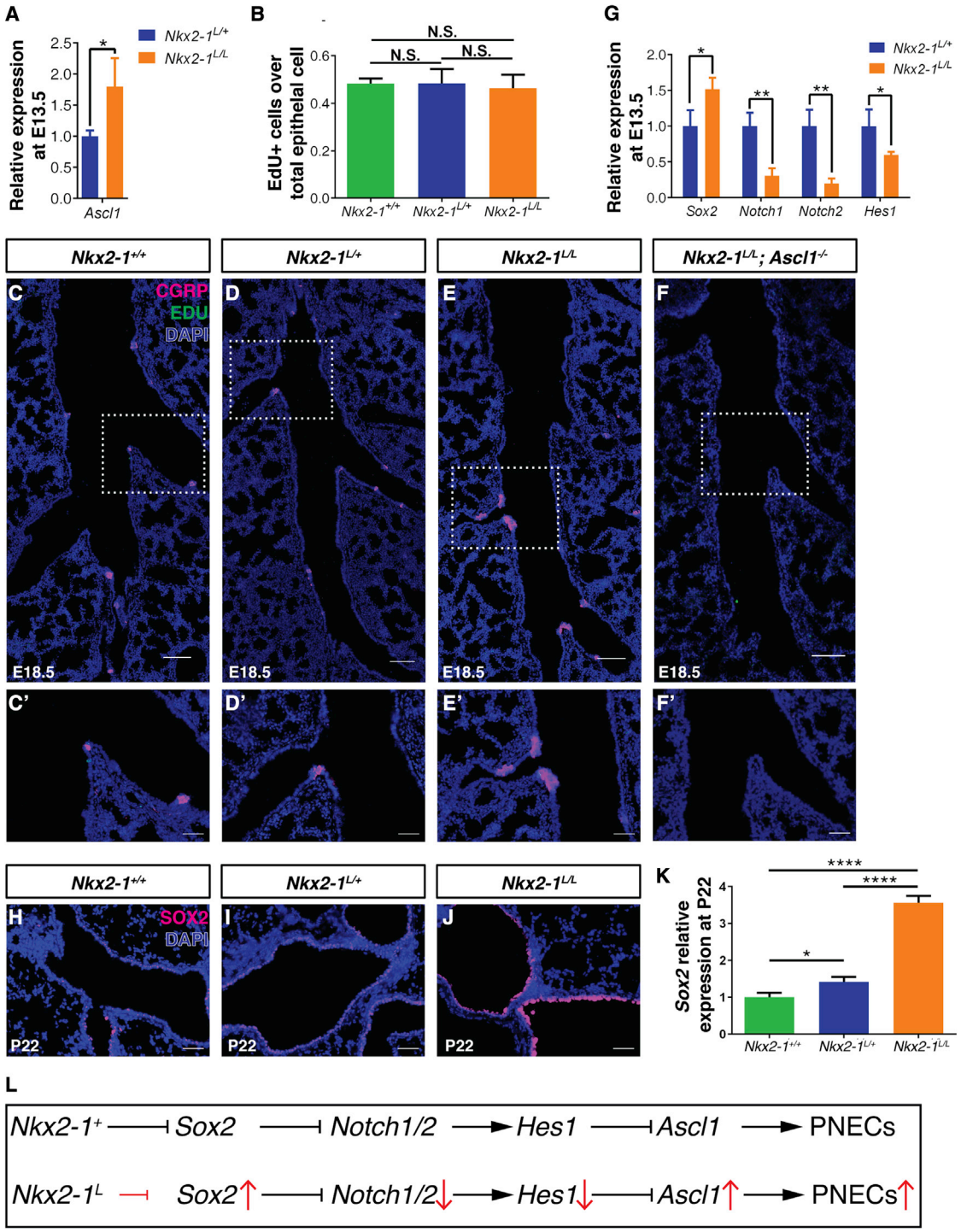


**Figure 2. PNEC hyperplasia in *Nkx2-1*$^{L/L}$ mutants is associated with increased *Sox2*, decreased Notch signaling, and increased specification rather than proliferation**

(A) qPCR showing increased PNEC marker *Ascl1* at E13.5 when PNECs are first specified (n = 3 for each group).

(B) Rate of epithelial cell proliferation quantified by EdU staining at E13.5 (n = 3 for each group).

(C–F) Representative longitudinal section of the main airway of E18.5 lungs with anti-CGRP antibody staining labeling PNECs. Scale bars, 100 μm. (C′–F′) Magnified view of boxed areas in (C–F), respectively. Scale bars, 50 μm.

(G) qPCR of *Sox2* and Notch pathway genes *Notch1*, *Notch2*, and *Hes1* at E13.5 (n = 3 for each group).

(H–J) Representative anti-SOX2 antibody staining at P22. Scale bars, 100 μm.

(K) qPCR of *Sox2* at P22 (n = 3 for each group).

*(legend continued on next page)*

Please cite this article in press as: Xu et al., Excess neuropeptides in lung signal through endothelial cells to impair gas exchange, Developmental Cell (2022), https://doi.org/10.1016/j.devcel.2022.02.023



MUC5AC (Figures S1G–S1K). Furthermore, in *Nkx2-1*$^{L/L}$ mutants, the expression of key type 2 immunity cytokines such as *Il5* and *Il13* remained normal, suggesting that there is no heightened immune phenotype, consistent with the lack of inflammation in NEHI patient lungs (Figure S1L). Analogous to NEHI patient lungs, *Nkx2-1*$^{L/L}$ mouse mutant lungs exhibit normal lung size, normal alveolar architecture as quantified by mean linear intercept (MLI), and normal distribution of alveolar type 1 and type 2 (AT1 and AT2) cells by both immunostaining and qRT-PCR analysis (Figures S1M–S1X).

Patients with NEHI have normal birth weight but frequently exhibit failure to thrive by a few months of age, thought to be attributed to their chronic respiratory disease including tachypnea and hypoxemia. Similarly, *Nkx2-1*$^{L/L}$ mutants had normal birth weight but displayed increasing growth retardation compared with littermate controls starting at P10 (Figures 1L and 1M). Importantly, *Nkx2-1*$^{L/L}$ mutants also exhibited low oxygen saturations as measured by $SpO_2$ (Figure 1N). Taken together, these observations indicate that the *Nkx2-1*$^{L/L}$ mouse mutants faithfully recapitulate key histological features and physiological symptoms observed in patients with NEHI, providing a mouse model of this disease.

## PNEC hyperplasia was associated with increased cell specification rather than proliferation

The mechanism underlying PNEC hyperplasia in NEHI has been debated, with consideration of increased cell specification versus increased proliferation of existing PNECs. To distinguish between these possibilities using the mouse model, we first determined the earliest time point when increased PNECs were detected by tracing the expression of *Ascl1*, a key PNEC cell fate marker. We found that *Ascl1* expression is already increased at embryonic day (E) 13.5, the stage when PNEC fate is normally specified (Figure 2A) (Kuo and Krasnow, 2015). However, by EdU labeling at this time point, there was no change in epithelial proliferation in *Nkx2-1*$^{L/L}$ lungs compared with control genotypes (Figure 2B).

As *Ascl1* is also essential for PNEC specification (Ito et al., 2000) to directly test the possibility that PNEC hyperplasia in this NEHI model is due to increased specification, we generated *Nkx2-1*$^{L/L}$*; Ascl1*$^{-/-}$ double mutants. The double mutant mice died at birth, likely due to known requirement for *Ascl1* outside of the lung (Ito et al., 2000). When analyzed just before birth at E18.5, the double mutants showed a complete absence of PNECs, including those in the airway and alveolar regions (Figures 2C–2F). Consistent with the dependence of ectopic alveolar PNECs on *Ascl1*, lineage-tracing using *Ascl1*$^{creER}$; *R26R*$^{LSL\text{-}tdTomato}$; and *Nkx2-1*$^{L/L}$ mice showed that the ectopic alveolar CGRP+ cells are derived from the *Ascl1* lineage (Figures S2A and S2B). Furthermore, these CGRP+ cells do not express HOPX or pro-SPC, markers for AT1 and AT2 cells, respectively, despite their localization in the alveolar region (Figures S2C and S2D). Collectively, these findings suggest that PNEC hyperplasia is due to increased *Ascl1*-dependent specification.

## *Nkx2-1*$^{L/L}$ mice exhibited increased expression of *Sox2* and decreased expression of Notch pathway genes, behaving as partial loss-of-function mutants

After establishing that the increase of *Ascl1* is responsible for PNEC hyperplasia, we next dissected the molecular pathway from *Nkx2-1*$^{L}$ mutation to *Ascl1* increase. Previous studies show that NKX2-1 represses the expression of *Sox2* (Domyan et al., 2011; Que et al., 2007). In turn, SOX2 inhibits the expression of *Notch*, and NOTCH activation induces the expression of *Hes1*, which inhibits the expression of *Ascl1* (Li et al., 2013; Xu et al., 2014). By qRT-PCR at E13.5, we observed an increase in *Sox2* and a decrease in Notch pathway genes including *Notch1*, *Notch2*, and *Hes1* in *Nkx2-1*$^{L/L}$ lungs (Figure 2G). This increase in SOX2 persisted in postnatal stages as validated by anti-SOX2 antibody staining and qRT-PCR (Figures 2H–2K). Tracking back to normal embryonic lung, there is a clear correlation between higher SOX2 expression and PNEC cell fate (Figure S2E). These results are consistent with a genetic pathway from *Nkx2-1* to *Sox2* to Notch signaling, resulting in regulation of *Ascl1* expression and PNEC specification (Figure 2L).

The direction of gene expression changes downstream of *Nkx2-1* suggests that *Nkx2-1*$^{L}$ is a loss-of-function allele and inactivation of *Nkx2-1* would lead to increased PNECs. This notion is counter to the report that PNECs were absent in the *Nkx2-1*$^{-/-}$ null mutant, which also exhibited an early halt in overall lung development (Li et al., 2013). To resolve this discrepancy, we bypassed the early requirement for *Nkx2-1* in lung specification and inactivated the gene just prior to PNEC specification. In *Nkx2-1*$^{creER/F}$ conditional mutants, we observed a significant upregulation of PNEC markers by both immunostaining and qRT-PCR analysis (Figures S2F–S2H).

To further confirm that *Nkx2-1*$^{L}$ is a loss-of-function allele, we performed a classical genetic complementation test by mating mice carrying the *Nkx2-1*$^{L}$ allele to mice carrying the *Nkx2-1*$^{-}$ null allele. PNEC increase was detected in *Nkx2-1*$^{L/-}$ mutants compared with controls while the lung size remained largely normal (Figures S2I–S2K). Unlike in *Nkx2-1* null mutants where trachea and esophagus failed to separate (Minoo et al., 1999), they separated normally in *Nkx2-1*$^{L/-}$ mutants. These results together suggest that *Nkx2-1*$^{L}$ acts as a partial loss-of-function allele.

## *Nkx2-1*$^{L/L}$ mutants developed excess fluid in lung

A key puzzle in NEHI is the cause of hypoxemia, given that lung size and alveolar architecture appear normal. Establishment of the animal model allowed us to investigate a range of parameters using invasive approaches in mutants compared with littermate controls. Since *Nkx2-1*$^{L/L}$ mutants showed improved body weight and oxygenation with age, similar as what has been reported in patients with NEHI (Figures S3A–S3F) (Deterding et al., 2005; Nevel et al., 2018). Therefore, we focused on early time points to evaluate potential pathophysiologic mechanisms. We found that the wet-to-dry (W/D) ratio of mutant lungs was

(L) Schematics of a molecular mechanism linking *Nkx2-1*$^{L}$ mutation to PNEC hyperplasia, as supported by data here and previous publications (Domyan et al., 2011; Ito et al., 2000; Li et al., 2013; Que et al., 2007; Xu et al., 2014).

Student's t test was used for (A and K). One-way ANOVA Tukey's multiple comparisons test was used for (B and K). N.S., not significant, $p \geq 0.05$. * for $p < 0.05$, ** for $p < 0.01$, **** for $p < 0.0001$. Error bars represent mean ± SD.

See also Figure S2.

Please cite this article in press as: Xu et al., Excess neuropeptides in lung signal through endothelial cells to impair gas exchange, Developmental Cell (2022), https://doi.org/10.1016/j.devcel.2022.02.023



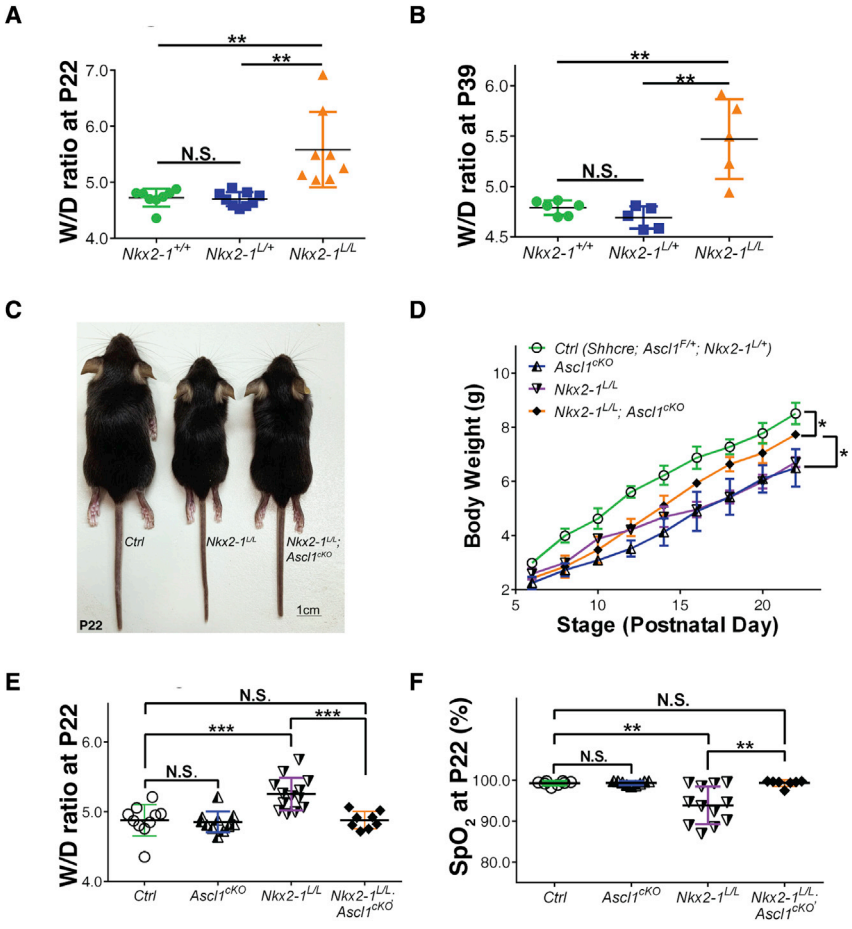


**Figure 3. PNEC hyperplasia is responsible for lung fluid increase and gas exchange deficiency**

(A and B) Lung W/D ratio at P22 ($n \geq 8$ for each group) and at P39 ($n \geq 5$ for each group).

(C) Representative body size at P22.

(D) Growth curve from P5 to P22 of 12 pups nursed by the same outbred foster mother (n = 3 for each group). Statistical analysis was carried out separately at each time point.

(E) Lung W/D ratio at P22 ($n \geq 8$ for each group).

(F) Oxygen saturation as measured by $SpO_2$ at P22 ($n \geq 7$ for each group).

One-way ANOVA Tukey's multiple comparisons test was used for (A and B), and two-way ANOVA Tukey's multiple comparisons test was used for (D–F). N.S., not significant, * for $p < 0.05$, ** for $p < 0.01$, *** for $p < 0.001$. Error bars represent mean ± SD. See also Figure S3.

statistically significantly increased at weaning (P22) and at the end of alveologenesis (P39) (Figures 3A and 3B). These data indicate that the overall excess fluid in lung is a quantifiable phenotype associated with the NEHI mouse model.

## Preventing PNEC formation alleviated excess fluid, reduced oxygenation, and growth defect in the NEHI mouse model

It has been long debated whether PNEC hyperplasia are causal for NEHI symptoms, are bystanders, or a consequence of the disease. To test these possibilities using the NEHI model, we genetically prevented the formation of PNECs in NEHI lung by generating *Nkx2-1*$^{L/L}$; *Shh*$^{cre/+}$; *Ascl1*$^{F/F}$ (hereafter referred to as *Nkx2-1*$^{L/L}$; *Ascl1*$^{cKO}$ mutant). As in *Nkx2-1*$^{L/L}$; *Ascl1*$^{-/-}$ mutant, inactivation of *Ascl1* led to a complete absence of PNECs in *Nkx2-1*$^{L/L}$; *Ascl1*$^{cKO}$ mutant (Figures S3G–S3I). However, unlike the *Ascl1*$^{-/-}$ mutant that died at birth due to global loss of *Ascl1*, the tissue-specific *Shh*$^{cre/+}$; *Ascl1*$^{F/F}$ mutant and thereby the *Nkx2-1*$^{L/L}$; *Ascl1*$^{cKO}$ mutant survived (Sui et al., 2018). We found that compound *Nkx2-1*$^{L/L}$; *Ascl1*$^{cKO}$ mutants displayed improved body weight, normal lung W/D ratio, and oxygen saturation level at P22 compared with either *Nkx2-1*$^{L/L}$ or *Ascl1*$^{cKO}$ single mutants (Figures 3C–3F). These findings demonstrate that rather than being the consequence of NEHI, PNECs are key contributors to excess fluid, hypoxemia, and growth retardation in the NEHI mouse model.

## Genetic inactivation of PNEC products alleviated excess fluid, reduced oxygenation, and growth defect in the NEHI mouse model

Next, we investigated the molecular mediators that link PNEC hyperplasia to NEHI-like phenotypes. As PNECs are known for their production of highly bioactive neuropeptides and neurotransmitters, we focused on these products. CGRP, a key neuropeptide secreted by PNECs, can induce edema when injected in the paw (Brain et al., 1985; Newbold and Brain, 1993). To address if CGRP plays a role in the *Nkx2-1*$^{L/L}$ physiological phenotypes, we measured CGRP levels in bronchioalveolar lavage (BAL) fluid and found significant increases in CGRP levels in in *Nkx2-1*$^{L/L}$ mutants compared with controls, suggesting that upregulated *Calca* (encoding CGRP) gene expression resulted in elevated secreted protein (Figure 4A). In addition, intranasal administration of CGRP in early postnatal pups led to increased W/D ratio (Figures 4B and 4C), indicating that excess CGRP is sufficient to cause excess fluid in lung.

To test if increased CGRP may contribute to NEHI phenotypes, we inactivated CGRP gene in NEHI mutants by generating *Nkx2-1*$^{L/L}$; *Calca*$^{-/-}$ double mutants. As expected, in these double mutants, PNEC hyperplasia was still observed, whereas CGRP was at background level by staining and in BAL fluid (Figures 4D and S4A–S4F). At P22, the *Nkx2-1*$^{L/L}$; *Calca*$^{-/-}$ double mutants displayed normal body weight, decreased lung W/D ratio, and normal oxygen saturation compared with those of single mutants and *Nkx2-1*$^{L/+}$ controls (Figures 4E–4H). We note that the W/D ratio did not fully revert back to control level, suggesting that other PNEC products may contribute to the excess fluid phenotype. In support of this, inactivation of *Tac1*—which encodes substance P, another edema-inducing neuropeptide (Newbold and Brain, 1993)—also led to partial reversal of the excess fluid phenotype in the *Nkx2-1*$^{L/L}$ mutant background (Figures S4G–S4I). These results indicate that PNEC products contribute significantly to

Please cite this article in press as: Xu et al., Excess neuropeptides in lung signal through endothelial cells to impair gas exchange, Developmental Cell (2022), https://doi.org/10.1016/j.devcel.2022.02.023



CellPress

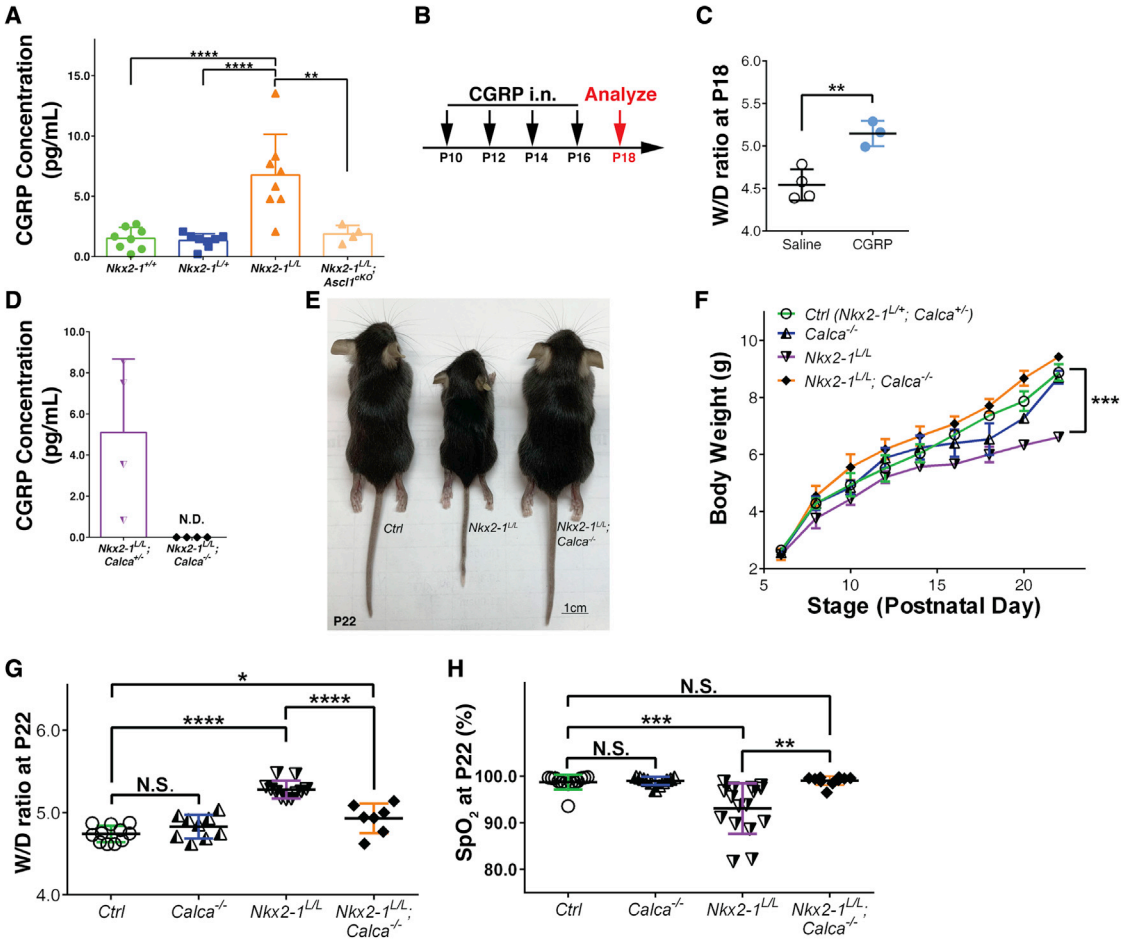


**Figure 4. PNEC product CGRP contributed to lung fluid increase and gas exchange deficiency**

(A) CGRP concentration in BAL as measured by ELISA for each genotype (n = 8 for first three groups, n = 4 for *Nkx2-1*$^{L/L}$; *Ascl1*$^{cKO}$ mutants).

(B) Wild-type mice were intranasally administrated with 10 μL 1 pg/μL CGRP or saline at P10, P12, P14, and P16. This concentration was selected based on physiological range measured by BAL ELISA.

(C) Lung W/D ratio measured at P18 (n = 4 for saline-treated group, n = 3 for CGRP-treated group).

(D) CGRP concentration in BAL as measured by ELISA for each genotype (n = 4 for each group).

(E) Representative body size at P22.

(F) Growth curve from P5 to P22 of 12 pups nursed by the same outbred foster mother (n = 3 for each group). Statistical analysis was carried out separately at each time point.

(G) Lung W/D ratio at P22 (n ≥ 7 for each group).

(H) Oxygen saturation at P22 (n ≥ 10 for each group).

One-way ANOVA Tukey's multiple comparisons test was used for (A). Student's t test was used for (C), and two-way ANOVA Tukey's multiple comparisons test was used for (F–H). N.S., not significant, $p \geq 0.05$. * for $p < 0.05$, ** for $p < 0.01$, *** for $p < 0.001$, **** for $p < 0.0001$. Error bars represent mean ± SD.

See also Figure S4.

excess fluid, reduced oxygen saturation, and poor weight gain in mice.

Our previous study showed that PNECs are important for amplifying asthmatic response including goblet cell metaplasia following exposure to allergen (Sui et al., 2018). Thus, we also addressed if PNECs are responsible for the goblet cell metaplasia phenotype in *Nkx2-1*$^{L/L}$ mutants. We confirmed this possibility by the finding that few goblet cells were detected in *Nkx2-1*$^{L/L}$; *Ascl1*$^{cKO}$ mutants (Figures S4J–S4M). We and others have shown that PNECs produce γ-aminobutyric acid (GABA), and GABA is required for allergen-induced goblet cell metaplasia phenotype (Barrios et al., 2017, 2019; Sui et al., 2018; Xiang et al., 2007). To address if GABA is responsible for goblet cell metaplasia phenotype in the *Nkx2-1*$^{L/L}$ mutants, we inactivated vesicular GABA transporter gene *Vgat* that is required for GABA secretion in the *Nkx2-1*$^{L/L}$ mutant background (*Nkx2-1*$^{L/L}$; *Shh*$^{cre/+}$; *Vgat*$^{F/F}$, hereafter referred to as *Nkx2-1*$^{L/L}$; *Vgat*$^{cKO}$ mutant). Few goblet cells were detected in *Nkx2-1*$^{L/L}$; *Vgat*$^{cKO}$ (Figures S4N and S4O). In contrast, goblet cell metaplasia persisted in *Nkx2-1*$^{L/L}$; *Calca*$^{-/-}$ mutants (Figures S4P and S4Q). Furthermore, pharmaceutical inhibition of $GABA_A$ receptor by antagonist bicuculline also alleviated the phenotype (Figures S4R–S4W). Taken together, our data indicate that GABA produced

Please cite this article in press as: Xu et al., Excess neuropeptides in lung signal through endothelial cells to impair gas exchange, Developmental Cell (2022), https://doi.org/10.1016/j.devcel.2022.02.023



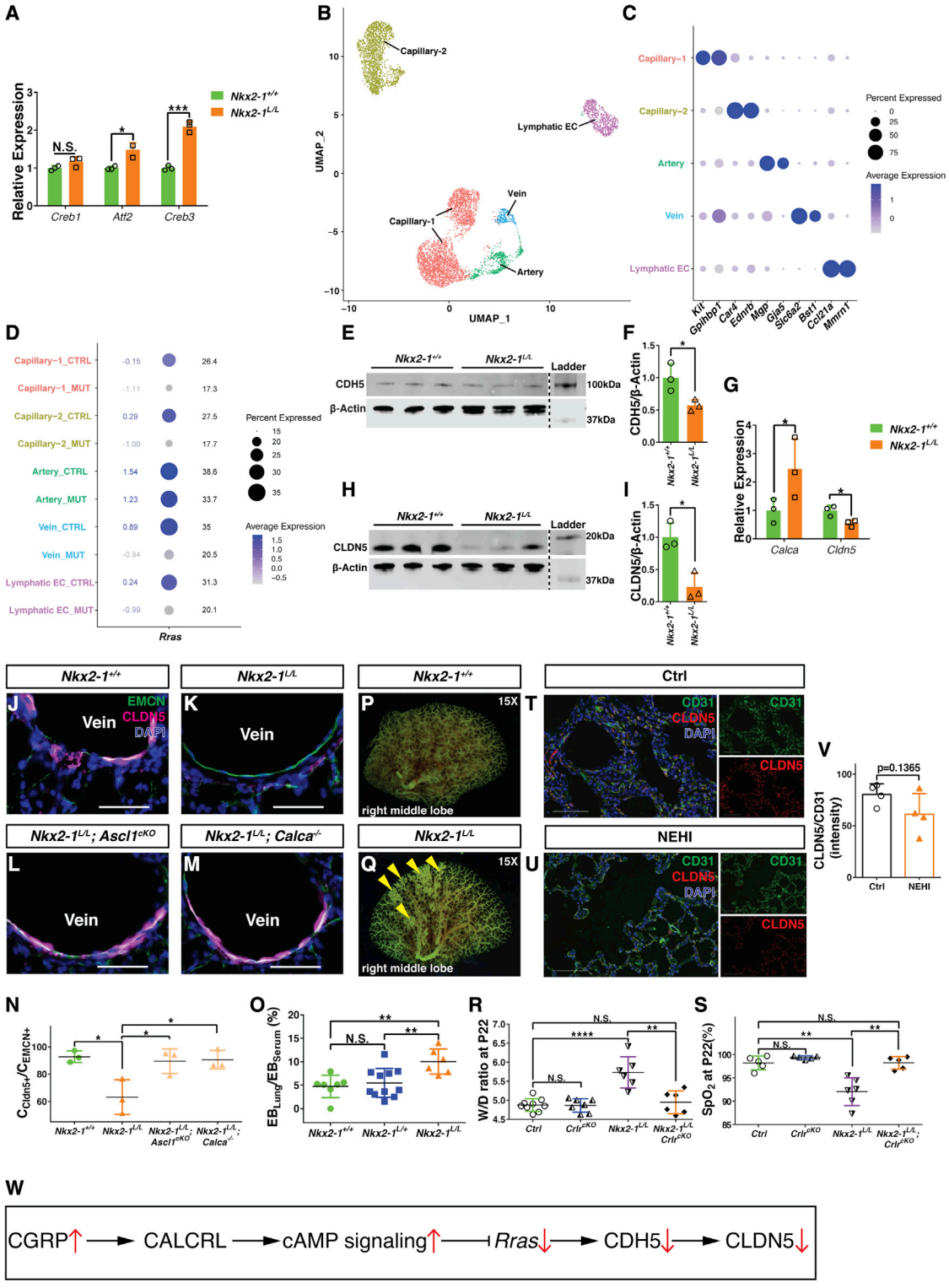


**Figure 5. Excess CGRP produced by PNECs signals to pulmonary endothelial cells and in turn leads to excess fluid and reduced oxygenation in the NEHI mouse model**

(A) qPCR of CGRP downstream cAMP signaling genes *Creb1*, *Atf2* (also termed *Creb2*), and *Creb3* in P22 whole lungs (n = 3 for each group).

(B) Integrated uniform manifold approximation and projection (UMAP) plot of scRNA-seq data of CD31+ endothelial cells isolated from P22 *Nkx2-1*$^{+/+}$ and *Nkx2-1*$^{L/L}$ lungs.

(C) Dot plot showing marker genes for each population.

*(legend continued on next page)*

Please cite this article in press as: Xu et al., Excess neuropeptides in lung signal through endothelial cells to impair gas exchange, Developmental Cell (2022), https://doi.org/10.1016/j.devcel.2022.02.023





by PNECs is a significant contributor to goblet cell metaplasia in the *Nkx2-1*$^{L/L}$ mutant.

### Increased CGRP acts through receptors on endothelial cells to downregulate junction protein expression, leading to disruption of barrier, excess fluid, and reduced oxygenation

Next, we investigated how increased PNECs and their products could contribute to excess fluid in lung. It is known that CGRP binding to receptors functions through activating cAMP signaling (Aiyar et al., 1996). Consistent with increased signaling in the *Nkx2-1*$^{L/L}$ mutant, whole lung qRT-PCR analysis showed upregulation of cAMP response element-binding protein (*Creb*) genes *Atf2* (also called *Creb2*) and *Creb3*, two effectors of cAMP signaling, whereas *Creb1* level was not significantly different from control (Figure 5A). To address how CGRP may contribute to excess fluid, we focused on endothelial cells because available single-cell RNA-seq (scRNA-seq) data indicate that in both mouse and human lungs, the expression of obligatory CGRP receptor gene *calcitonin receptor-like* (*Calcrl*, or *Crlr*) is highly enriched in all subpopulations of endothelial cells (Figures S5A–S5D) (Du et al., 2017; Travaglini et al., 2020; Wang et al., 2020). We generated scRNA-seq data using both Mut (*Nkx2-1*$^{L/L}$) and Ctrl (*Nkx2-1*$^{+/+}$) lungs at P22, which captured all major endothelial cell types (Figures 5B and 5C). Cell-cell communication analysis revealed a clear PNEC-endothelial signaling signature, highlighted by CGRP-CALCRL pairing (Figures S5E–S5G). Among the top differentially expressed genes is *Rras*, a key cAMP-regulated downstream effector gene. In the *Nkx2-1*$^{L/L}$ mutant lung, *Rras* is downregulated in multiple endothelial cell populations, including vein and both capillary populations (Figure 5D). This is consistent with data from endothelium cell culture showing that prolonged activation of CREB signaling reduces *Rras* level (Perrot et al., 2018).

Results from endothelium culture experiments also showed that prolonged cAMP activation, functioning through repressing *Rras*, disrupts adherence junction VE-cadherin (also called CDH5) function, leading to increased endothelium permeability (Perrot et al., 2018). Previous studies also showed that CDH5 can regulate endothelium-specific tight junction factors such as *Cldn5* with a critical role in endothelium barrier maintenance in lung (Jang et al., 2011; Taddei et al., 2008). These findings led us to assess junctional proteins and endothelium permeability in the *Nkx2-1*$^{L/L}$ mutant lung. We found that compared with control, the mutant lungs showed quantitatively reduced CDH5 protein by western blot analysis (Figures 5E and 5F), reduced *Cldn5* gene expression by qRT-PCR, and reduced CLDN5 protein by western blot analysis as well as by immunostaining (Figures 5G–5K). Interestingly, immunostaining also showed that such CLDN5 downregulation was no longer apparent in endothelial cells of the *Nkx2-1*$^{L/L}$; *Ascl1*$^{cKO}$ or *Nkx2-1*$^{L/L}$; *Calca*$^{-/-}$ compound mutants, where wet-dry ratio and other physiological abnormalities were attenuated (Figures 5L–5N). To assess barrier integrity, we introduced Evans blue dye into the blood stream and assayed for dye retention in lung following an established barrier assay protocol (Smith et al., 2019). The mutant lungs showed increased dye retention compared with control lungs, indicative of disrupted barrier and increased leakage (Figure 5O).

CGRP is a known vessel dilator and may contribute to excess fluid by allowing more fluid in vessels (Brain and Grant, 2004). To address if vessel engorgement may be a reason for excess fluid in the NEHI mutant lung, we performed angiogram assay by injecting dye into the vessels. We found that vessel size and number remained largely normal in the mutant compared with control (Figures S5H–S5J). Interestingly, in a subset of the lobes in the mutants (n = 3/4 animals) but not in controls (n = 0/3 animals), we also detected regional leakage in the distal vessels shortly

(D) Dot plot of *Rras* expression in individual endothelial population showing a decrease in vein, lymphatics, and both capillary populations in the Mut (*Nkx2-1*$^{L/L}$) compared with Ctrl (*Nkx2-1*$^{+/+}$) lungs. Numbers on the left denote expression levels, whereas numbers on the right denote percentages of cells within each equivalent cell types expressing *Cldn5*.
(E) CDH5 protein level as assayed by western blot of P22 lungs. Dashed line denotes a cut from the original blot.
(F) Quantification of CDH5 protein level after normalization to internal control β-actin level (n = 3 for each group).
(G) qRT-PCR confirming increased *Calca* and showing decreased *Cldn5* in P22 mutant versus control lungs.
(H) CLDN5 protein level assayed by western blot of P22 lungs. Dashed line denotes a cut from the original blot.
(I) Quantification of CLDN5 protein level in whole lungs after normalization to internal control β-actin level (n = 3 for each group).
(J–M) Anti-CLDN5 antibody staining (magenta) and anti-Endomucin (EMCN) antibody staining for vein cells (green) showed reduced CLDN5 expression in *Nkx2-1*$^{L/L}$ mutants compared with *Nkx2-1*$^{+/+}$ controls (J and K). *Nkx2-1*$^{L/L}$; *Ascl1*$^{cKO}$ and *Nkx2-1*$^{L/L}$; *Calca*$^{-/-}$ compound mutants showed similar CLDN5 pattern as *Nkx2-1*$^{+/+}$ controls (L and M). Scale bar: 50 μm.
(N) Percentage of the vessel circumference outlined by EMCN staining that was also CLDN5+ (n = 3 for each group).
(O) Lung Evans blue level as a ratio of dye retained in lung versus level in serum (n ≥ 6 for each group).
(P and Q) Representative whole mount angiogram images of right middle lobes of *Nkx2-1*$^{+/+}$ (P) and *Nkx2-1*$^{L/L}$ (Q) mice at P22 where leakage was observed in the mutant lung. Magnification: 15×. Leaking regions were marked by yellow arrowheads in (Q).
(R) Lung W/D ratio at P22 (n ≥ 6 for each group).
(S) Oxygen saturation at P22 (n ≥ 5 for each group).
(T and U) Representative anti-CD31 antibody (green) and anti-CLDN5 antibody double staining (red) showed a decrease of CLDN5 in human NEHI patient biopsies (U) compared with normal lung biopsies (T). Scale bar: 100 μm.
(V) CLDN5/CD31 intensity ratio showing a trending decrease of ratio in NEHI biopsies compared with control (n = 4 for each group).
(W) Schematics of a molecular mechanism linking increased CGRP and disrupted endothelial integrity in *Nkx2-1*$^{L/L}$ mutants, as supported by data here and previous publications (Aiyar et al., 1996; Jang et al., 2011; Perrot et al., 2018; Taddei et al., 2008; Travaglini et al., 2020; Wang et al., 2020).
Student's t test was used for (A, F, G, I, and V). One-way ANOVA Tukey's multiple comparisons test was used for (N and O). Two-way ANOVA Tukey's multiple comparisons test was used for (R and S). N.S., not significant, $p \geq 0.05$. ** for $p < 0.05$, ** for $p < 0.01$, *** for $p < 0.001$, **** for $p < 0.0001$. Error bars represent mean ± SD.
See also Figure S5 and Table S1.

Please cite this article in press as: Xu et al., Excess neuropeptides in lung signal through endothelial cells to impair gas exchange, Developmental Cell (2022), https://doi.org/10.1016/j.devcel.2022.02.023



after dye injection, consistent with results from Evans blue assay (Figures 5P and 5Q). These findings together raised the possibility that a breach of barrier may contribute to excess fluid in the *Nkx2-1*$^{L/L}$ mutant.

To test directly if excess CGRP signaling on endothelial cells could contribute to NEHI phenotypes *in vivo*, we inactivated *Crlr* specifically in endothelial cells by generating *Nkx2-1*$^{L/L}$; *Cdh5-cre*; *Crlr*$^{F/F}$ compound mutants (hereafter referred to as *Nkx2-1*$^{L/L}$; *Crlr*$^{cKO}$ mutant). *Nkx2-1*$^{L/L}$; *Crlr*$^{cKO}$ mutants exhibited normal lung W/D ratio and oxygen saturation, demonstrating that signaling via CRLR receptor on endothelial cells contributed significantly to NEHI physiological phenotypes in *Nkx2-1*$^{L/L}$ mutants (Figures 5R and 5S).

To test if similar barrier disruption occurs in patients with NEHI, we performed immunofluorescence staining on normal and NEHI lung biopsies. Expected increase of PNECs was captured by staining for specification marker PROX1 in NEHI biopsies compared with the control (Figures S5K and S5L). Although not reaching statistical significance likely due to variability in human genetic background, age, fixation conditions used at the time of procurement, and lengths of storage, there was a trend toward decrease of CLDN5/CD31 intensity ratio in NEHI biopsies compared with controls (Figures 5T–5V and S5M–S5P), suggesting a potential downregulation of tight junction proteins in human NEHI lungs. Taken together with data from our NEHI mouse model, our findings support a role of excess CGRP in downregulating junctional proteins, compromising pulmonary endothelial barrier, leading to reduced oxygenation (Figure 5W).

### Pharmacological inhibition of CGRP signaling alleviated excess fluid, reduced oxygenation, and growth defect in the NEHI mouse model

Findings from gene expression and genetic compound mutants suggest that repressing CGRP may be effective at attenuating abnormalities observed in the NEHI mouse model. To test this concept directly, we inhibited CGRP function locally by intranasal administration of BIBN-4096, a CGRP receptor antagonist at the postnatal stage (Figure 6A). Compared with vehicle DMSO treatment, BIBN-4096 treatment in the control genotype groups did not lead to detectable effects. In comparison, in *Nkx2-1*$^{L/L}$ mutants, BIBN-4096 treatment led to a clear attenuation of all key NEHI physiological phenotypes, including excess lung fluid, reduced oxygen saturation, and poor weight gain (Figures 6B–6D). By performing qPCR analyses, we found that the attenuation of physiological phenotypes was linked to reversal of molecular changes, including a downregulation of cAMP signaling as marked by *Atf2* expression level upon BIBN-4096 treatment (Figures S6A–S6D). Additionally, qPCR, western blot, and immunostaining showed a reversal of CLDN5 RNA and protein levels and a trending reversal of CDH5 protein level in BIBN-4096-treated *Nkx2-1*$^{L/L}$ mutants compared with the DMSO-treated vesicle control group (Figures 6E–6J). These results demonstrate the efficacy of CGRP receptor antagonist in treating NEHI symptoms in this animal model.

To address if increase of PNEC products such as CGRP may be relevant in other disease conditions with excess lung fluid, we investigated signaling changes in coronavirus disease 2019 (COVID-19) associated ARDS lungs, which feature excess fluid as the primary cause of death (Ackermann et al., 2020; Fox et al., 2020). We found that in lungs from patients who have succumbed to COVID-19, a majority of PNECs, as identified by their expression of GRP (also known as Bombesin), expressed CGRP (81.35% ± 4.686%, n = 7 donors, Table S2 for donor metadata). There is a statistically significant increase ($p < 0.0001$ and $p = 0.0012$, respectively) over the proportion of PNECs expressing CGRP in non-ARDS controls from either surgical samples (19.34% ± 7.259%, n = 4 donors) or autopsy samples (39.03% ± 8.135%, n = 4 donors) (Figures 7A–7F). Furthermore, we also detected high CGRP+ PNECs (74.93% ± 1.668%, n = 3 donors) in non-COVID ARDS samples (Figures 7G–7I). Consistent with the link between CGRP increase and CLDN5 downregulation in both *Nkx2-1*$^{L/L}$ mutants and NEHI biopsies (Figure 5), a significant decrease of CLDN5+ endothelial cells were also detected in ARDS samples (53.88% ± 24.67%, n = 3 donors) compared with surgical (91.30% ± 5.908%, n = 3 donors) or autopsy 88.02% ± 6.656%, n = 4 donors) samples (Figures 7J–7P). A significant downregulation of CLDN5 was also reported in COVID-19 lung samples (D'Agnillo et al., 2021). Although excessive lung damage and inflammation are likely the primary cause of profound damage in COVID and non-COVID ARDS, the staining data combined with our functional findings from the NEHI mouse model raised the possibility that increased PNEC production of neuropeptides may be an additional contributor to excess lung fluid in these conditions.

## DISCUSSION

In this study, we present evidence from *in vivo* experiments demonstrating a fundamental mechanism of neuropeptidergic control of pulmonary vascular integrity and, in turn, oxygenation. Increased PNECs and their secreted neuropeptides are necessary and sufficient to cause excess fluid in lung and compromised oxygenation. Given the absence of alveolar structural disruption and overt immune infiltration, the *Nkx2-1* mutant NEHI mouse model provides a streamlined experimental platform to evaluate the specific effects of PNEC-derived neuropeptides on lung function. The discovered mechanism is supported by several modes of robust *in vivo* rescues of NEHI phenotypes, including prevention of PNEC formation, inactivation of CGRP, endothelium-specific inactivation of CGRP receptor, and treatment with CGRP receptor antagonist.

Starting with a *NKX2-1* variant reported in a multigeneration familial cohort with NEHI, this mouse model of the disease has revealed step-by-step links from the candidate NEHI gene to cellular, molecular, and physiological phenotypes (Figures 2L, 5W, and 7Q). The finding that disrupting PNEC formation in the *Nkx2-1* mutant background reversed NEHI phenotypes addresses a long-standing debate and demonstrates that PNEC hyperplasia is a driver of symptoms.

We demonstrated that this particular *Nkx2-1* associated with NEHI is a partial loss-of-function allele. Reduced *Nkx2-1* function led to increased *Sox2* expression, decreased Notch signaling, and increased *Ascl1* expression (Figure 2L). Results from the *Nkx2-1*$^{L/L}$; *Ascl*$^{-/-}$ double mutant show that increased *Ascl1* is responsible for increased PNECs. Data from scRNA-seq, qRT-PCR, western blot analysis, and antibody staining demonstrate that with increased PNECs, excess PNEC products such as

Please cite this article in press as: Xu et al., Excess neuropeptides in lung signal through endothelial cells to impair gas exchange, Developmental Cell (2022), https://doi.org/10.1016/j.devcel.2022.02.023



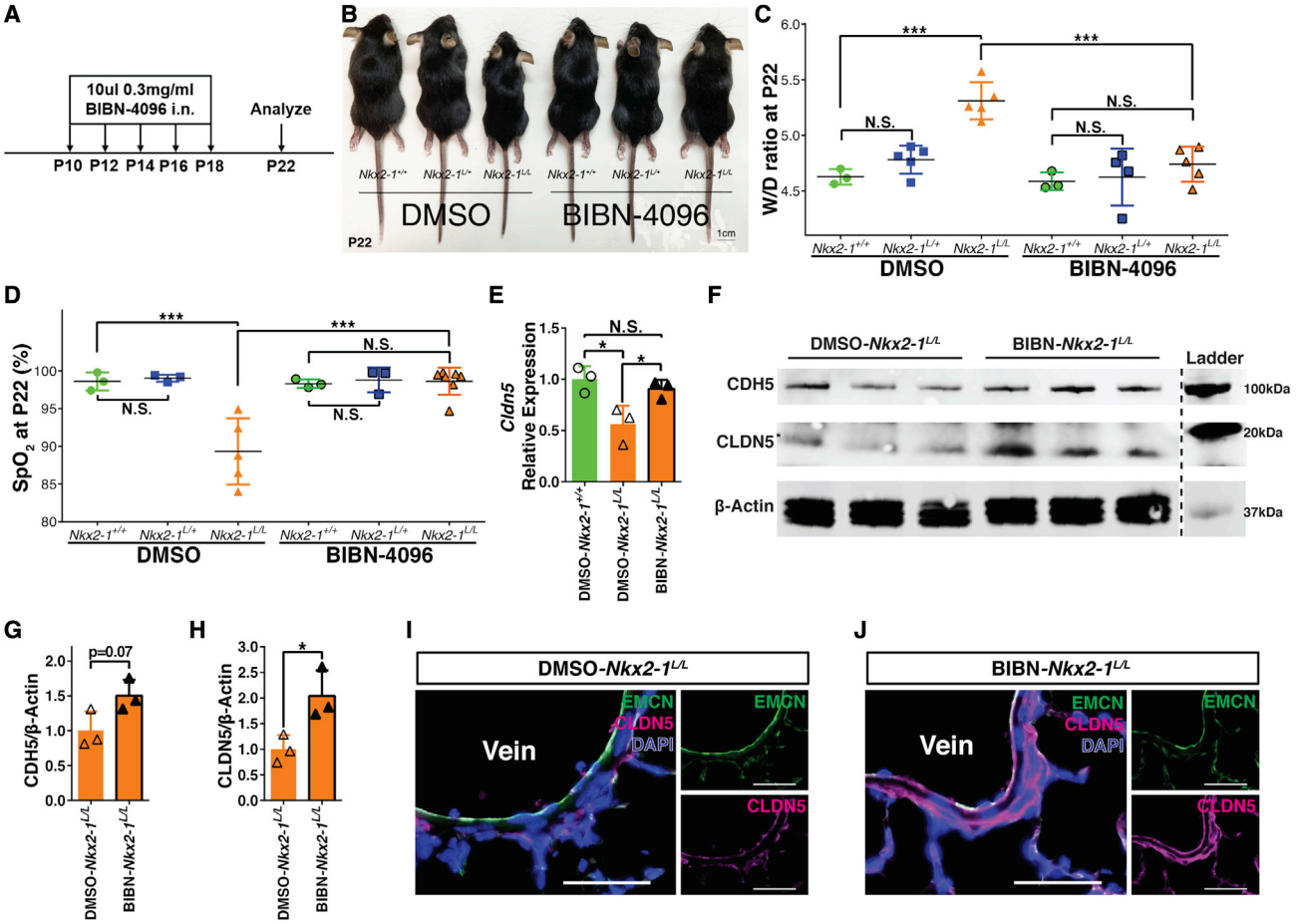


**Figure 6. Antagonizing CGRP signaling reversed molecular changes, alleviated excess fluid and reduced oxygenation in the NEHI mouse model**

(A) Regime of intranasal BIBN-4096 administration. The dose was selected based on published literature (Aubdool et al., 2014).

(B) Representative body size comparison at P22. All individuals were nursed by the same foster mother.

(C) Lung W/D ratio at P22 ($n \geq 3$ for each group).

(D) Oxygen saturation at P22 ($n \geq 3$ for each group).

(E) qPCR of *Cldn5* at P22, n = 3 for each group.

(F–H) CDH5 and CLDN5 protein levels in P22 lungs as assayed by western blot. Dashed line denotes a cut from the original blot. Quantifications were shown in (G and H), respectively. n =3 for each group.

(I and J) Representative anti-CLDN5 antibody staining (magenta) and anti-EMCN antibody staining for vein cells (green) showed restored CLDN5 level in BIBN-treated *Nkx2-1*$^{L/L}$ mutants compared with DMSO-treated *Nkx2-1*$^{L/L}$ mutants.

Two-way ANOVA Tukey's multiple comparisons test was used for (C and D). One-way ANOVA Tukey's multiple comparisons test was used for (E). Student's t test was used for (G and H). N.S., not significant, $p \geq 0.05$. * for $p < 0.05$, *** for $p < 0.001$. Error bars represent mean ± SD.

See also Figure S6.

CGRP signal to endothelial cells, resulting in prolonged activation of G protein coupled receptor (GPCR) and downstream cAMP signaling, which lead to downregulation of Rras and junctional proteins essential for barrier maintenance (Figure 5W). A disruption of barrier is supported by increased Evans blue dye retention and increased angiogram dye leakage. Across the various compound mutants, the tight association of changes in wet/dry ratio, reduced oxygen saturations, and growth retardation parameters suggest that these phenotypes are likely linked (Figure 7Q). It remains possible that other mechanisms may contribute to these NEHI phenotypes. Regardless of the relationship among poor gas exchange, excess lung fluid, and decreased growth rate, the findings that disruption of neuropeptide signaling can reverse these defects demonstrates a significant role of neuropeptides in normal lung physiology.

Results in the present study uncovered a critical *in vivo* role of PNECs in regulating lung fluid. We note that the wet/dry ratio increase in the NEHI mouse model is mild in comparison with that in animal models of ARDS (Gotts et al., 2019). We postulate that in NEHI, it is possible that vessel leakage and fluid accumulation is concentrated at small bronchiole/alveolar entrance areas near common sites of PNEC hyperplasia. This could explain how a limited increase in fluid volume could block gas exchange in a relatively large alveolar areas distal to blockage points, effectively reducing oxygenation. This possibility is consistent with the dye leakage pattern near distal vessels in the angiograms

Please cite this article in press as: Xu et al., Excess neuropeptides in lung signal through endothelial cells to impair gas exchange, Developmental Cell (2022), https://doi.org/10.1016/j.devcel.2022.02.023



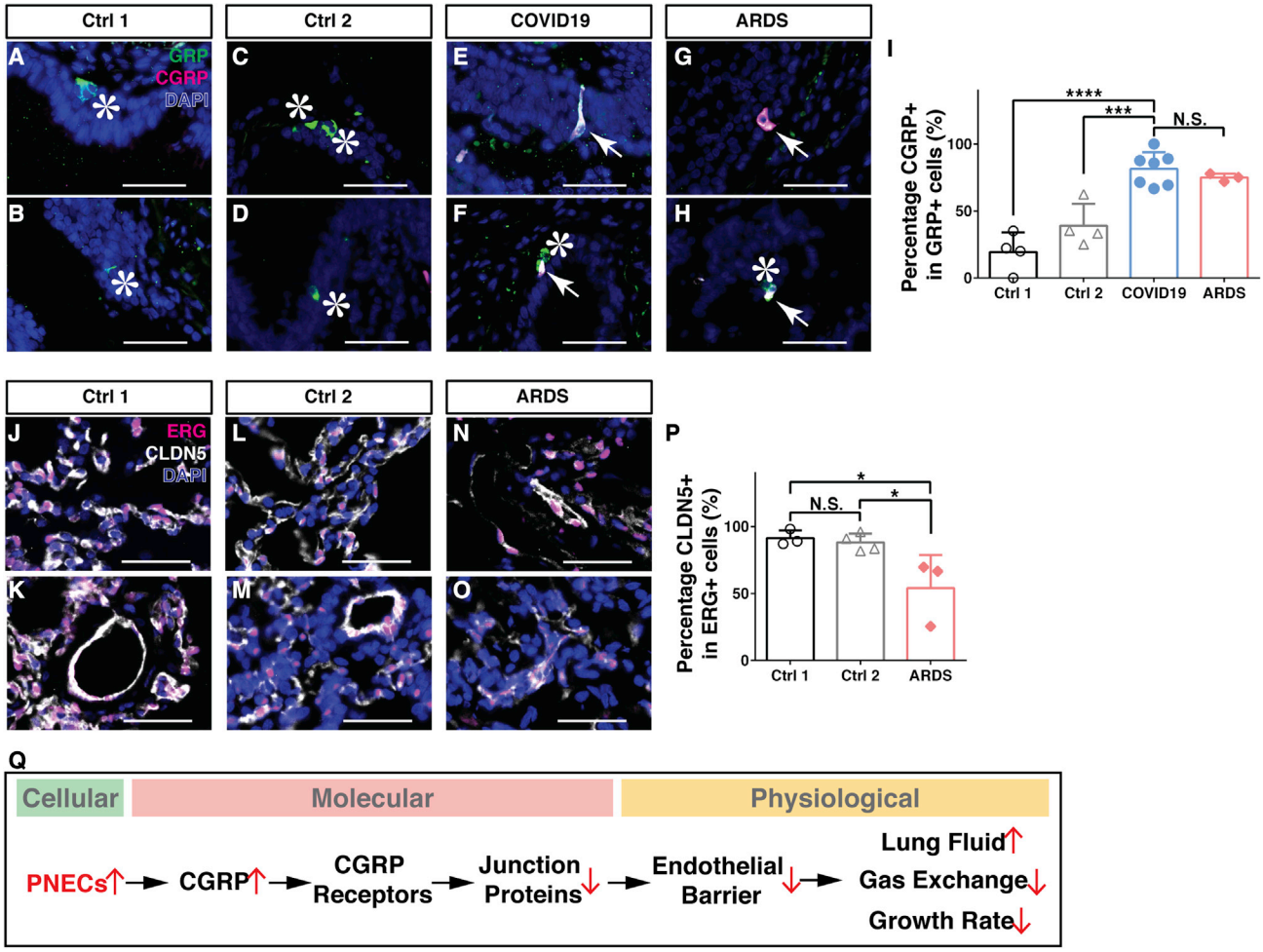


**Figure 7. Human ARDS lungs exhibit increased proportion of CGRP+ PNECs and reduced tight junction protein expression**

(A–H) Examples of anti-GRP staining (green, pan-PNEC marker) and anti-CGRP staining (magenta) showed differential proportion of CGRP+ PNECs in different groups of donor lungs. Ctrl 1: controls from lobectomy tissues without notable lung pathology (A and B), Ctrl 2: controls from autopsy tissues without notable lung pathology (C and D), COVID-19 ARDS samples (E and F), and non-COVID-19 ARDS samples (G and H). Asterisks indicate CGRP-negative PNECs; arrows indicate CGRP-positive PNECs.

(I) Percentages of CGRP+ PNECs in all GRP+ PNECs in noted sample groups. Each dot represents averaged data from one donor across multiple sections.

(J–O) Representative images of anti-ERG staining (magenta, endothelial marker) and anti-CLDN5 staining (white) showed decrease of CLDN5 level in non-COVID-19 ARDS samples. Ctrl 1 (J and K), Ctrl 2 (L and M), and ARDS (N and O) groups are the same as described in (A–H).

(P) Percentages of CLDN5+ cells in ERG+ endothelial cells in noted sample groups. Each dot represents averaged data from one donor across multiple sections.

(Q) A model for PNEC function in the control of lung fluid balance. In NEHI, PNEC hyperplasia led to increased neuropeptides such as CGRP, which signal to pulmonary endothelial cells to disrupt barrier integrity, leading to excess extravascular lung fluid as well as gas exchange deficiency.

One-way ANOVA Tukey's multiple comparisons test was used for (P and I). N.S., not significant, $p \geq 0.05$. * for $p < 0.05$, ** for $p < 0.01$, *** for $p < 0.001$, **** for $p < 0.0001$. Error bars represent mean ± SD.

See also Table S2.

of NEHI mouse model. Local airway obstruction by fluid could also contribute to unexplained clinical findings in patients with NEHI, including crackles on chest auscultation as well as chest imaging that demonstrates hyperinflation and distinctive ground-glass opacities without architectural distortion (Young et al., 2011). Further studies are needed to understand how these murine model alterations in barrier and vascular integrity relate to findings in the human disease, although it is intriguing to consider the possibility that fluid homeostasis could be relevant.

We found that in the lungs of patients who succumbed to COVID-19 or non-COVID-19 ARDS, there was increased proportion of PNECs expressing CGRP. Increased substance P was also found in the pulmonary edema fluids of ARDS patients as well as a sheep model of ARDS (Espiritu et al., 1992). Our result that substance P-encoding *Tac1* null mutation can rescue NEHI phenotypes suggest that substance P may also play a notable role in inducing excess lung fluid. There are many known causes of ARDS, including infection induced damage and inflammation (Huppert et al., 2019; Matthay et al., 2019). Our findings here raise the possibility that neuropeptide-induced barrier disruption may serve as another molecular contributor. Forms of CGRP or CGRP receptor antagonists have been approved by US Food

and Drug Administration (FDA) for the treatment of migraine, paving the way for considering them a candidate treatment for conditions with excess fluid in lung (Olesen et al., 2004). In light of the knowledge that CGRP has vessel dilator activity, the potential effect of CGRP antagonism in exacerbating vessel constriction was addressed in their safe use in the treatment for migraine (Breen et al., 2021; MaassenVanDenBrink et al., 2016) and should also be carefully considered in their potential use for treating other diseases associated with excess neuropeptides.

Our study reaffirms the notion that investigating rare diseases can lead to discoveries of fundamental biological mechanisms. From NEHI, we uncovered that neuropeptides regulate lung fluid level and, in turn, gas exchange efficiency. Aside from PNECs, neuropeptides such as CGRP and substance P can also be produced by nerves in the lung (Baral et al., 2018; Hennessy et al., 2017; Su et al., 2022). Outside of the lung, neuroendocrine cells and nerves are present in many peripheral tissues such as the intestine, stomach, prostate, etc. (Kaelberer et al., 2018; Xu et al., 2020). Future studies are needed to address if excess neuropeptide signaling may be a recurrent contributor to disease conditions with excess tissue fluid.

### Limitations of the study

Although our NEHI mouse model captured key characteristics of the disease, there are remaining human patient features (e.g., crackles on chest auscultation) that cannot be reliably detected and rigorously investigated in mice. Overall, documented physiological differences between human and mouse should be taken into consideration when interpreting physiological data from mice. Lastly, limited access to human samples (including NEHI and ARDS lung biopsies) has restrained our ability to quantitatively determine the link between increased neuropeptides and impaired endothelial barrier. This link could be further interrogated by obtaining and assaying tissues from additional donors.

## STAR★METHODS

Detailed methods are provided in the online version of this paper and include the following:

- KEY RESOURCES TABLE
- RESOURCE AVAILABILITY
  - Lead contact
  - Materials availability
  - Data and code availability
- EXPERIMENTAL MODEL AND SUBJECT DETAILS
  - Mice
  - Human donors and tissue collection
- METHOD DETAILS
  - Histology preparation, periodic acid–Schiff (PAS) staining, and mean linear intercept (MLI) quantification
  - Immunofluorescent staining
  - Immunofluorescent staining and quantification on control and NEHI lung biopsies
  - EdU analysis for cell proliferation
  - Oxygen saturation ($SpO_2$) measurement
  - Lung wet-to-dry ratio measurement
  - Bronchoalveolar lavage (BAL)
  - ELISA
  - Tissue dissociation and sorting of single cells
  - Droplet-based high throughput single-cell RNA-seq and data analysis
  - Western blot analysis
  - Evans Blue dye assay
  - Mouse lung angiogram
  - CGRP, BIBN-4096, and Bicuculline intranasal administration
- QUANTIFICATION AND STATISTICAL ANALYSIS
  - Quantitative PCR (qPCR)

## SUPPLEMENTAL INFORMATION

Supplemental information can be found online at https://doi.org/10.1016/j.devcel.2022.02.023.

## ACKNOWLEDGMENTS

The authors would like to thank members of the Sun lab for inputs and discussions. This work was supported by NIH R01HL146141 (to X.S. and L.R.Y.), NIH OT2OD023857 (to X.S.), ATS Research Foundation 2019-1059 (to X.S.), Orphan Disease Center MDBR-21-115-NEHI (to X.S. and L.R.Y), and AHA predoctoral fellowship 828448 (to J.X.). Single-cell RNA-seq was performed using the service of UC San Diego IGM Genomics Center utilizing an Illumina NovaSeq 6000 that was purchased with funding from a National Institutes of Health SIG grant (#S10 OD026929). Cell sorting was performed using the Flow Cytometry Core at the San Diego Center for AIDS Research (P30 AI036214), the VA San Diego Health Care System, and the San Diego Veterans Medical Research Foundation. We also thank the UCSD School of Medicine Microscopy Core (National Institute of Neurological Disorders and Stroke grant P30 NS047101) for assistance with imaging and analysis.

## AUTHOR CONTRIBUTIONS

J.X., X.S., and L.R.Y. conceived and designed experiments. J.X. and X.S. interpreted data. J.X., L.X., P.S., J.C., E.A.M., P.H., W.J.J., J.M.D., P.T., A.C., P.G., B.B., M.K.G., L.C.-A., and G.D. performed experiments and provided tissues. J.X. and L.X. analyzed single-cell RNA-seq data and generated figures. A.M., G.P., G.D., L.R.Y., and X.S. provided supervision and support. J.X. and X.S. wrote the manuscript with input from the other authors.

## DECLARATION OF INTERESTS

X.S. is a member of the advisory board for *Developmental Cell*. J.X., L.R.Y., and X.S. have one related Patent Cooperation Treaty (PCT) application approved by World Intellectual Property Organization (WIPO) with number WO2020252368.

Received: August 25, 2021
Revised: February 2, 2022
Accepted: February 23, 2022
Published: March 17, 2022

## REFERENCES

Ackermann, M., Verleden, S.E., Kuehnel, M., Haverich, A., Welte, T., Laenger, F., Vanstapel, A., Werlein, C., Stark, H., Tzankov, A., et al. (2020). Pulmonary vascular endothelialitis, thrombosis, and angiogenesis in Covid-19. N. Engl. J. Med. *383*, 120–128.

Aiyar, N., Rand, K., Elshourbagy, N.A., Zeng, Z., Adamou, J.E., Bergsma, D.J., and Li, Y. (1996). A cDNA encoding the calcitonin gene-related peptide type 1 receptor. J. Biol. Chem. *271*, 11325–11329.

Aubdool, A.A., Graepel, R., Kodji, X., Alawi, K.M., Bodkin, J.V., Srivastava, S., Gentry, C., Heads, R., Grant, A.D., Fernandes, E.S., et al. (2014). TRPA1 is

essential for the vascular response to environmental cold exposure. Nat. Commun. *5*, 5732.

Baral, P., Umans, B.D., Li, L., Wallrapp, A., Bist, M., Kirschbaum, T., Wei, Y., Zhou, Y., Kuchroo, V.K., Burkett, P.R., et al. (2018). Nociceptor sensory neurons suppress neutrophil and γδ T cell responses in bacterial lung infections and lethal pneumonia. Nat. Med. *24*, 417–426.

Barrios, J., Kho, A.T., Aven, L., Mitchel, J.A., Park, J.A., Randell, S.H., Miller, L.A., Tantisira, K.G., and Ai, X. (2019). Pulmonary neuroendocrine cells secrete gamma-aminobutyric acid to induce goblet cell hyperplasia in primate models. Am. J. Respir. Cell Mol. Biol. *60*, 687–694.

Barrios, J., Patel, K.R., Aven, L., Achey, R., Minns, M.S., Lee, Y., Trinkaus-Randall, V.E., and Ai, X. (2017). Early life allergen-induced mucus overproduction requires augmented neural stimulation of pulmonary neuroendocrine cell secretion. FASEB J. *31*, 4117–4128.

Brain, S.D., and Grant, A.D. (2004). Vascular actions of calcitonin gene-related peptide and adrenomedullin. Physiol. Rev. *84*, 903–934.

Brain, S.D., Williams, T.J., Tippins, J.R., Morris, H.R., and MacIntyre, I. (1985). Calcitonin gene-related peptide is a potent vasodilator. Nature *313*, 54–56.

Breen, I.D., Brumfiel, C.M., Patel, M.H., Butterfield, R.J., VanderPluym, J.H., Griffing, L., Pittelkow, M.R., and Mangold, A.R. (2021). Evaluation of the safety of calcitonin gene-related peptide antagonists for migraine treatment among adults with Raynaud phenomenon. JAMA Netw. Open *4*, e217934.

Chintagari, N.R., and Liu, L. (2012). GABA receptor ameliorates ventilator-induced lung injury in rats by improving alveolar fluid clearance. Crit. Care *16*, R55.

Cutz, E., Yeger, H., and Pan, J. (2007). Pulmonary neuroendocrine cell system in pediatric lung disease-recent advances. Pediatr. Dev. Pathol. *10*, 419–435.

D'Agnillo, F., Walters, K.A., Xiao, Y., Sheng, Z.M., Scherler, K., Park, J., Gygli, S., Rosas, L.A., Sadtler, K., Kalish, H., et al. (2021). Lung epithelial and endothelial damage, loss of tissue repair, inhibition of fibrinolysis, and cellular senescence in fatal COVID-19. Sci. Transl. Med. *13*, eabj7790.

Deterding, R.R., Pye, C., Fan, L.L., and Langston, C. (2005). Persistent tachypnea of infancy is associated with neuroendocrine cell hyperplasia. Pediatr. Pulmonol. *40*, 157–165.

Domyan, E.T., Ferretti, E., Throckmorton, K., Mishina, Y., Nicolis, S.K., and Sun, X. (2011). Signaling through BMP receptors promotes respiratory identity in the foregut via repression of Sox2. Development *138*, 971–981.

Du, Y., Kitzmiller, J.A., Sridharan, A., Perl, A.K., Bridges, J.P., Misra, R.S., Pryhuber, G.S., Mariani, T.J., Bhattacharya, S., Guo, M., et al. (2017). Lung gene expression analysis (LGEA): an integrative web portal for comprehensive gene expression data analysis in lung development. Thorax *72*, 481–484.

Espiritu, R.F., Pittet, J.F., Matthay, M.A., and Goetzl, E.J. (1992). Neuropeptides in pulmonary edema fluid of adult respiratory distress syndrome. Inflammation *16*, 509–517.

Fox, S.E., Akmatbekov, A., Harbert, J.L., Li, G., Quincy Brown, J., and Vander Heide, R.S. (2020). Pulmonary and cardiac pathology in African American patients with COVID-19: an autopsy series from New Orleans. Lancet Respir. Med. *8*, 681–686.

Fritz-Six, K.L., Dunworth, W.P., Li, M., and Caron, K.M. (2008). Adrenomedullin signaling is necessary for murine lymphatic vascular development. J. Clin. Invest. *118*, 40–50.

Gotts, J.E., Bernard, O., Chun, L., Croze, R.H., Ross, J.T., Nesseler, N., Wu, X., Abbott, J., Fang, X., Calfee, C.S., and Matthay, M.A. (2019). Clinically relevant model of pneumococcal pneumonia, ARDS, and nonpulmonary organ dysfunction in mice. Am. J. Physiol. Lung Cell. Mol. Physiol. *317*, L717–L736.

Hennessy, M.L., Corcoran, A.E., Brust, R.D., Chang, Y., Nattie, E.E., and Dymecki, S.M. (2017). Activity of Tachykinin1-expressing Pet1 raphe neurons modulates the respiratory chemoreflex. J. Neurosci. *37*, 1807–1819.

Huppert, L.A., Matthay, M.A., and Ware, L.B. (2019). Pathogenesis of acute respiratory distress syndrome. Semin. Respir. Crit. Care Med. *40*, 31–39.

Ito, T., Udaka, N., Yazawa, T., Okudela, K., Hayashi, H., Sudo, T., Guillemot, F., Kageyama, R., and Kitamura, H. (2000). Basic helix-loop-helix transcription factors regulate the neuroendocrine differentiation of fetal mouse pulmonary epithelium. Development *127*, 3913–3921.

Jang, A.S., Concel, V.J., Bein, K., Brant, K.A., Liu, S., Pope-Varsalona, H., Dopico, R.A., Jr., Di, Y.P., Knoell, D.L., Barchowsky, A., and Leikauf, G.D. (2011). Endothelial dysfunction and claudin 5 regulation during acrolein-induced lung injury. Am. J. Respir. Cell Mol. Biol. *44*, 483–490.

Jin, S., Guerrero-Juarez, C.F., Zhang, L., Chang, I., Ramos, R., Kuan, C.H., Myung, P., Plikus, M.V., and Nie, Q. (2021). Inference and analysis of cell-cell communication using CellChat. Nat. Commun. *12*, 1088.

Kaelberer, M.M., Buchanan, K.L., Klein, M.E., Barth, B.B., Montoya, M.M., Shen, X., and Bohórquez, D.V. (2018). A gut-brain neural circuit for nutrient sensory transduction. Science *361*, eaat5236.

Kuo, C.S., and Krasnow, M.A. (2015). Formation of a neurosensory organ by epithelial cell slithering. Cell *163*, 394–405.

Kusakabe, T., Kawaguchi, A., Hoshi, N., Kawaguchi, R., Hoshi, S., and Kimura, S. (2006). Thyroid-specific enhancer-binding protein/NKX2.1 is required for the maintenance of ordered architecture and function of the differentiated thyroid. Mol. Endocrinol. *20*, 1796–1809.

Li, C., Li, A., Xing, Y., Li, M., Chan, B., Ouyang, R., Taketo, M.M., Kucherlapati, R., Borok, Z., and Minoo, P. (2013). Apc deficiency alters pulmonary epithelial cell fate and inhibits Nkx2.1 via triggering TGF-beta signaling. Dev. Biol. *378*, 13–24.

Liptzin, D.R., Pickett, K., Brinton, J.T., Agarwal, A., Fishman, M.P., Casey, A., Towe, C.T., Taylor, J.B., Kurland, G., Hagood, J.S., et al. (2020). Neuroendocrine cell hyperplasia of infancy. Clinical score and comorbidities. Ann. Am. Thorac. Soc. *17*, 724–728.

Maassenvandenbrink, A., Meijer, J., Villalón, C.M., and Ferrari, M.D. (2016). Wiping out CGRP: potential cardiovascular risks. Trends Pharmacol. Sci. *37*, 779–788.

Matthay, M.A., Zemans, R.L., Zimmerman, G.A., Arabi, Y.M., Beitler, J.R., Mercat, A., Herridge, M., Randolph, A.G., and Calfee, C.S. (2019). Acute respiratory distress syndrome. Nat. Rev. Dis. Primers *5*, 18.

Minoo, P., Su, G., Drum, H., Bringas, P., and Kimura, S. (1999). Defects in tracheoesophageal and lung morphogenesis in *Nkx2.1*(−/−)mouse embryos. Dev. Biol. *209*, 60–71.

Moitra, J., Sammani, S., and Garcia, J.G. (2007). Re-evaluation of Evans blue dye as a marker of albumin clearance in murine models of acute lung injury. Transl. Res. *150*, 253–265.

Nevel, R.J., Garnett, E.T., Schaudies, D.A., and Young, L.R. (2018). Growth trajectories and oxygen use in neuroendocrine cell hyperplasia of infancy. Pediatr. Pulmonol. *53*, 656–663.

Newbold, P., and Brain, S.D. (1993). The modulation of inflammatory oedema by calcitonin gene-related peptide. Br. J. Pharmacol. *108*, 705–710.

Ochs, M., Nyengaard, J.R., Jung, A., Knudsen, L., Voigt, M., Wahlers, T., Richter, J., and Gundersen, H.J. (2004). The number of alveoli in the human lung. Am. J. Respir. Crit. Care Med. *169*, 120–124.

Olesen, J., Diener, H.C., Husstedt, I.W., Goadsby, P.J., Hall, D., Meier, U., Pollentier, S., and Lesko, L.M.; BIBN 4096 BS Clinical Proof of Concept Study Group (2004). Calcitonin gene-related peptide receptor antagonist BIBN 4096 BS for the acute treatment of migraine. N. Engl. J. Med. *350*, 1104–1110.

Pacary, E., Heng, J., Azzarelli, R., Riou, P., Castro, D., Lebel-Potter, M., Parras, C., Bell, D.M., Ridley, A.J., Parsons, M., and Guillemot, F. (2011). Proneural transcription factors regulate different steps of cortical neuron migration through Rnd-mediated inhibition of RhoA signaling. Neuron *69*, 1069–1084.

Perrot, C.Y., Sawada, J., and Komatsu, M. (2018). Prolonged activation of cAMP signaling leads to endothelial barrier disruption via transcriptional repression of RRAS. FASEB J. *32*, fj201700818RRR.

Que, J., Okubo, T., Goldenring, J.R., Nam, K.T., Kurotani, R., Morrisey, E.E., Taranova, O., Pevny, L.H., and Hogan, B.L. (2007). Multiple dose-dependent roles for Sox2 in the patterning and differentiation of anterior foregut endoderm. Development *134*, 2521–2531.

Schneider, C.A., Rasband, W.S., and Eliceiri, K.W. (2012). NIH Image to ImageJ: 25 years of image analysis. Nat. Methods *9*, 671–675.

Smith, P., Jeffers, L.A., and Koval, M. (2019). Effects of different routes of endotoxin injury on barrier function in alcoholic lung syndrome. Alcohol *80*, 81–89.

Su, Y., Barr, J., Jaquish, A., Xu, J., Verheyden, J.M., and Sun, X. (2022). Identification of lung innervating sensory neurons and their target specificity. Am. J. Physiol. Lung Cell. Mol. Physiol. *322*, L50–L63.

Sui, P., Wiesner, D.L., Xu, J., Zhang, Y., Lee, J., Van Dyken, S., Lashua, A., Yu, C., Klein, B.S., Locksley, R.M., et al. (2018). Pulmonary neuroendocrine cells amplify allergic asthma responses. Science *360*, eaan8546.

Taddei, A., Giampietro, C., Conti, A., Orsenigo, F., Breviario, F., Pirazzoli, V., Potente, M., Daly, C., Dimmeler, S., and Dejana, E. (2008). Endothelial adherens junctions control tight junctions by VE-cadherin-mediated upregulation of claudin-5. Nat. Cell Biol. *10*, 923–934.

Travaglini, K.J., Nabhan, A.N., Penland, L., Sinha, R., Gillich, A., Sit, R.V., Chang, S., Conley, S.D., Mori, Y., Seita, J., et al. (2020). A molecular cell atlas of the human lung from single-cell RNA sequencing. Nature *587*, 619–625.

Wang, A., Chiou, J., Poirion, O.B., Buchanan, J., Valdez, M.J., Verheyden, J.M., Hou, X., Kudtarkar, P., Narendra, S., Newsome, J.M., et al. (2020). Single-cell multiomic profiling of human lungs reveals cell-type-specific and age-dynamic control of SARS-CoV2 host genes. eLife *9*, e62522.

Xiang, Y.-Y., Wang, S., Liu, M., Hirota, J.A., Li, J., Ju, W., Fan, Y., Kelly, M.M., Ye, B., Orser, B., et al. (2007). A GABAergic system in airway epithelium is essential for mucus overproduction in asthma. Nat. Med. *13*, 862–867.

Xiong, M., Jain, P.P., Chen, J., Babicheva, A., Zhao, T., Alotaibi, M., Kim, N.H., Lai, N., Izadi, A., Rodriguez, M., et al. (2021). Mouse model of experimental pulmonary hypertension: lung angiogram and right heart catheterization. Pulm. Circ. *11*, 20458940211041512.

Xu, J., Yu, H., and Sun, X. (2020). Less is more: rare pulmonary neuroendocrine cells function as critical sensors in lung. Dev. Cell *55*, 123–132.

Xu, X., Huang, L., Futtner, C., Schwab, B., Rampersad, R.R., Lu, Y., Sporn, T.A., Hogan, B.L., and Onaitis, M.W. (2014). The cell of origin and subtype of K-Ras-induced lung tumors are modified by Notch and Sox2. Genes Dev. *28*, 1929–1939.

Young, L.R., Brody, A.S., Inge, T.H., Acton, J.D., Bokulic, R.E., Langston, C., and Deutsch, G.H. (2011). Neuroendocrine cell distribution and frequency distinguish neuroendocrine cell hyperplasia of infancy from other pulmonary disorders. Chest *139*, 1060–1071.

Young, L.R., Deutsch, G.H., Bokulic, R.E., Brody, A.S., and Nogee, L.M. (2013). A mutation in TTF1/NKX2.1 is associated with familial neuroendocrine cell hyperplasia of infancy. Chest *144*, 1199–1206.

Zhu, Z., Wang, Y., Long, A., Feng, T., Ocampo, M., Chen, S., Tang, H., Guo, Q., Minshall, R., Makino, A., et al. (2020). Pulmonary vessel casting in a rat model of monocrotaline-mediated pulmonary hypertension. Pulm. Circ. *10*, 2045894020922129.

Please cite this article in press as: Xu et al., Excess neuropeptides in lung signal through endothelial cells to impair gas exchange, Developmental Cell (2022), https://doi.org/10.1016/j.devcel.2022.02.023



## STAR★METHODS

### KEY RESOURCES TABLE

| REAGENT or RESOURCE | SOURCE | IDENTIFIER |
|---|---|---|
| **Antibodies** | | |
| Mouse monoclonal anti-beta-actin | Novus | Cat# NB600-501; RRID: AB_10077656 |
| Rat monoclonal anti-CDH5 | BD Biosciences | Cat# 562795; RRID: AB_2737800 |
| Rabbit polyclonal anti-Calcitonin Gene Related Peptide (CGRP) | Sigma-Aldrich | Cat# C8198; RRID: AB_259091 |
| Mouse monoclonal anti-CLDN5 | Thermo Fisher Scientific | Cat# 35-2500, RRID: AB_2533200 |
| Mouse monoclonal anti-FOXJ1 | Thermo Fisher Scientific | Cat# 14-9965-80; RRID: AB_1548836 |
| Mouse monoclonal anti-HOPX | Santa Cruz | Cat# sc-398703; RRID: AB_2687966 |
| Mouse monoclonal anti- MUC5AC | Sigma-Aldrich | Cat# 929M-9 |
| Rabbit polyclonal anti-NKX2-1 (TTF1) | Seven Hills Bioreagents | Cat# WRAB-1231; RRID: AB_2832953 |
| Rabbit polyclonal anti-SCGB1A1 | Seven Hills Bioreagents | Cat # WRAB-3950 |
| Rabbit polyclonal anti-pro-SPC | Sigma-Aldrich | Cat# AB3786 |
| Mouse monoclonal anti-SOX2 | Santa Cruz | Cat# sc-365823; RRID: AB_10842165 |
| Rabbit polyclonal anti-Synaptophysin (SYP) | Fisher Scientific | Cat# RB-1461-P1; RRID: AB_60083 |
| Rabbit polyclonal anti-bombesin | ImmunoStar | Cat# 20073; RRID: AB_572221 |
| Mouse monoclonal anti-human CD31 | Agilent | Cat# GA610; RRID: AB_2892053 |
| Mouse monoclonal anti-human CD31 | Agilent | Cat# GA610; RRID: AB_2892053 |
| Rabbit monoclonal anti-human CLDN-5 | Thermo Fisher Scientific | Cat# MA5-32614; RRID: AB_2809891 |
| Rabbit monoclonal anti-ERG | Abcam | Cat# ab92513, RRID: AB_2630401 |
| Goat polyclonal anti-Human PROX1 | R&D Systems | Cat# AF2727; RRID: AB_2170716 |
| PE anti-mouse CD31 (PECAM-1) antibody | BioLegend | Cat# 160203; RRID: AB_2860750 |
| Brilliant Violet 510 (TM) anti-mouse CD45 antibody | BioLegend | Cat# 103137; RRID: AB_2561392 |
| APC anti-mouse CD326 (Ep-CAM) antibody | BioLegend | Cat# 118214; RRID: AB_1134102 |
| Rat Anti-CD16 / CD32 Monoclonal Antibody, Unconjugated | BD Biosciences | Cat# 553141; RRID: AB_394656 |
| Goat anti-mouse FITC | Jackson Immuno research Labs | Cat# 115-095-166, RRID: AB_2338601 |
| Goat anti-rabbit FITC | Thermo Fisher Scientific | Cat# A-11008; RRID: AB_143165 |
| Donkey anti-rat AF488 | Jackson Immuno research Labs | Cat# 712-545-150; RRID: AB_2340683 |
| Goat anti-mouse Cy3 | Jackson Immuno research Labs | Cat# 115-165-003; RRID: AB_2338680 |
| Goat anti-rabbit Cy3 | Jackson Immuno research Labs | Cat# 111-165-003; RRID: AB_2338000 |
| Goat anti-mouse Cy5 | Jackson Immuno research Labs | Cat# 115-175-166; RRID: AB_2338714 |
| Donkey anti–mouse IRDye 680RD | LI-COR | Cat# 925-69072 |
| Goat anti-rat IRDye 680LT | LI-COR | Cat# 925-68029 |
| **Critical commercial assays** | | |
| Chromium single cell RNA sequencing chemistry kit v3 | 10X Genomics | N/A |
| **Chemicals, peptides, and recombinant proteins** | | |
| Tamoxifen | Sigma-Aldrich | T5648, CAS 10540-29-1 |
| Click-iT™ EdU Cell Proliferation Kit | Thermo Fisher Scientific | Cat# C10337 |
| CGRP (Rat) EIA Kit | Cayman Chemicals | Cat# 589001 |
| DMSO | Sigma-Aldrich | Cat# D2650 |
| Synthesized CGRP | Sigma-Aldrich | Cat# C0292 |
| BIBN-4096 | Fisher Scientific | Cat# 45-611-0 |
| Bicuculline | Fisher Scientific | Cat# 01-305-0 |

(*Continued on next page*)

Please cite this article in press as: Xu et al., Excess neuropeptides in lung signal through endothelial cells to impair gas exchange, Developmental Cell (2022), https://doi.org/10.1016/j.devcel.2022.02.023





*Continued*

| REAGENT or RESOURCE | SOURCE | IDENTIFIER |
|---|---|---|
| MICROFIL® Silicone Rubber Injection Compounds | Flow-Tech Inc. | Cat# MV122 |
| Methyl Salicylate | Sigma-Aldrich | Cat# M6752 |
| DAPI | Sigma-Aldrich | Cat# D9542 |
| **Deposited data** | | |
| P22 Ctrl mice and NEHI mutants endothelial and epithelial cells single-cell RNA-seq data | This paper | GEO: GSE171907 |
| P22 Ctrl mice, NEHI mutants and BIBN-treated NEHI mutants western blot raw data | This paper | Mendeley Data: https://doi.org/10.17632/yk3hztpt49.1 |
| **Experimental models: Organisms/strains** | | |
| Mouse: Ai14, B6.Cg-Gt(ROSA) 26Sor$^{tm14(CAG-tdTomato)Hze}$/J | The Jackson Laboratory | JAX: 007914 |
| Mouse: Ascl1$^{creER}$, Ascl1$^{tm1.1(Cre/ERT2)Jejo}$/J | The Jackson Laboratory | JAX: 012882 |
| Mouse: Ascl1$^{Fl}$, Ascl1$^{tm2Fgu}$ | Guoli Dai, Francois Guillemot | (Pacary et al., 2011) |
| Mouse: Calca$^{-}$, B6.129P2(Cg)-Calca$^{tm1.1(EGFP/HBEGF)Mjz}$/Mmnc | MMRRC | RRID: MMRRC_036773-UNC |
| Mouse: Crlr$^{Fl}$, Calcrl$^{tm1Kmca}$ | Kathleen Caron | (Fritz-Six et al., 2008) |
| Mouse: Cdh5-cre, B6;129-Tg(Cdh5-cre) 1Spe/J | The Jackson Laboratory | JAX: 017968 |
| Mouse: Tac1$^{-}$, B6.Cg-Tac1$^{tm1Bbm}$/J | The Jackson Laboratory | JAX: 004103 |
| Mouse: Nkx2-1$^{creER}$, Nkx2-1$^{tm1.1(cre/ERT2)Zjh}$/J | The Jackson Laboratory | JAX: 014552 |
| Mouse: Nkx2-1$^{R161L}$ | This paper | N/A |
| Mouse: Nkx2-1$^{Fl}$, Nkx2-1$^{tm2Shk}$ | Shioko Kimura | (Kusakabe et al., 2006) |
| Mouse: Shh$^{cre}$, B6.129S6-Shh$^{tm2(cre/ERT2)Cjt}$/J | Cliff Tabin | JAX: 005623 |
| **Oligonucleotides** | | |
| qPCR Primer: Actb Forward: CGGCCAGGTCATCACTATTGGCAAC | This paper | N/A |
| qPCR Primer: Actb Reverse: GCCACAGGATTCCATACCCAAGAAG | This paper | N/A |
| qPCR Primer: Ascl1 Forward: TCTGGCAAGATGGAGAGTGGAGC | This paper | N/A |
| qPCR Primer: Ascl1 Reverse: AAAGAAGCAGGCTGCGGGAG | This paper | N/A |
| qPCR Primer: Atf2 Forward: GAGGAGCCTTCTGTTGTAGAAAC | This paper | N/A |
| qPCR Primer: Atf2 Reverse: GACGAACGATAGCTGATGTGG | This paper | N/A |
| qPCR Primer: Calca Forward: CCTTTCCTGGTTGTCAGCATCTTG | This paper | N/A |
| qPCR Primer: Calca Reverse: CTGGGCTGCTTTCCAAGATTGAC | This paper | N/A |
| qPCR Primer: Cldn5 Forward: ACGGGAGGAGCGCTTTAC | This paper | N/A |
| qPCR Primer: Cldn5 Reverse: GTTGGCGAACCAGCAGAG | This paper | N/A |
| A complete list of qPCR primers can be found in Table S3. | | |
| **Software and algorithms** | | |
| ImageJ | (Schneider et al., 2012) | https://imagej.nih.gov/ij/ |
| Prism 6 | Graph Pad Software | https://www.graphpad.com/scientific-software/prism/ |

(*Continued on next page*)

Please cite this article in press as: Xu et al., Excess neuropeptides in lung signal through endothelial cells to impair gas exchange, Developmental Cell (2022), https://doi.org/10.1016/j.devcel.2022.02.023



*Continued*

| REAGENT or RESOURCE | SOURCE | IDENTIFIER |
|---|---|---|
| Seurat V3 | Satija Lab | https://satijalab.org/seurat/ |
| CellChat | (Jin et al., 2021) | https://github.com/sqjin/CellChat |

## RESOURCE AVAILABILITY

### Lead contact

Further information and requests for resources and reagents should be directed to and will be fulfilled by the lead contact, Dr. Xin Sun (xinsun@health.ucsd.edu).

### Materials availability

Mice carrying the *Nkx2-1*$^{R161L}$ allele will be made available upon request following standard signing of Materials Transfer Agreement in accordance with NIH Principles and Guidelines.

### Data and code availability

- All raw sequencing data and processed files have been deposited in GEO under the series reference GEO: GSE171907 and are publicly available upon publication. Accession numbers are listed in the key resources table. Original western blot images have been deposited at Mendeley and are publicly available upon publication. The DOI is listed in the key resources table. Microscopy data reported in this paper will be shared by the lead contact upon request.
- This study does not report original code. All codes and algorithms used for single-cell RNA-seq analyses are listed in the key resources table.
- Any additional information required to reanalyze the data reported in this paper is available from the lead contact upon request.

## EXPERIMENTAL MODEL AND SUBJECT DETAILS

### Mice

All mice were housed in American Association for Accreditation of Laboratory Animal Care (AAALAC) accredited facilities and labs at University of California, San Diego. All animal husbandry and experiments were conducted under approved Institutional Animal Care and Use Committee (IACUC) guidelines. *Nkx2-1*$^{R161L}$ mouse line was designed and generated in the Sun's lab, with the service of the University of Wisconsin-Madison Transgenic Core. *Ascl1*$^{creERT2}$, *Cdh5-cre*, *Nkx2-1*$^{creERT2}$, *Tac1*$^{-}$, *Vgat*$^{fl}$, and Ai14 (*R26R*$^{LSL\text{-}tdTomato}$) mice were purchased from JAX. *Calca*$^{-}$ was obtained from MMRRC-UNC. *Ascl1*$^{fl}$ was a kind gift from Dr. Guoli Dai with permission from Dr. Francois Guillemot. *Crlr*$^{fl}$ was a kind gift from Dr. Kathleen Caron. *Nkx2-1*$^{fl}$ was a kind gift from Dr. Shioko Kimura. *Shh*$^{cre}$ was a kind gift from Dr. Cliff Tabin. All mice were either bred in B6 background or have been back crossed to B6 background for at least 3 generations. Littermates were used as controls to minimize potential genetic background effects. Data from male and female mice were pooled into one group for analysis unless otherwise noted.

### Human donors and tissue collection

Biopsies from 4 patients with the clinical and pathologic diagnosis of neuroendocrine cell hyperplasia of infancy and 4 age-matched control lungs (biopsied for other lung processes or from lobectomies with histologically normal lung adjacent to focal lesions; see Table S1 for metadata) were identified from a pathology database under a protocol approved by Seattle Children's Hospital Institutional Review Board.

Adult donor lung samples were procured under institutional approved protocols from the federal United Network of Organ Sharing via National Disease Research Interchange (NDRI) and International Institute for Advancement of Medicine (IIAM), at University of Rochester, University of California San Diego, or University of Colorado. Lungs were obtained from deceased donors who were either free of lung disease (n=4, non-ARDS autopsy controls), or succumbed to complications related to severe ARDS prior to COVID-19 pandemic (n=3, non-COVID-ARDS), or severe ARDS as a result of COVID-19 (n=7, COVID-ARDS). Lobectomy tissues without pathological lesion were collected as additional controls (n=4, non-ARDS lobectomy controls). Immunostaining was performed on fixed paraffin embedded lung samples. All tissues were obtained following fulfilment of institutionally approved informed consent protocol in each case.

## METHOD DETAILS

### Histology preparation, periodic acid–Schiff (PAS) staining, and mean linear intercept (MLI) quantification

Mice were euthanized under approved Institutional Animal Care and Use Committee (IACUC) guidelines. Lungs were inflated with 4% PFA at 35cm $H_2O$ airway pressure, fixed overnight and then prepared for paraffin (6μm) or cryo (10∼15 μm) sections. Goblet cells were stained using a periodic acid–Schiff (PAS) staining kit (Sigma). To quantify mean linear intercept (MLI), 10X H&E images

Please cite this article in press as: Xu et al., Excess neuropeptides in lung signal through endothelial cells to impair gas exchange, Developmental Cell (2022), https://doi.org/10.1016/j.devcel.2022.02.023





were used. For each group, 3 mice per genotype, 3 sections per mouse and 3 independent fields per section were analyzed. Samples were compared using Student's t-test, by MLI ± S.D. with statistical significance called at $p<0.05$.

### Immunofluorescent staining

The following primary antibodies were used at the indicated final concentration for immunofluorescence staining: rabbit anti-Synaptophysin polyclonal antibody [5 mg/ml] (Fisher), rabbit anti-Calcitonin gene-related peptide (CGRP) polyclonal antibody [2 mg/ml] (Sigma), rabbit anti-SCGB1A1 polyclonal antibody [5 mg/ml] (Seven Hills Bioreagents), rabbit anti-SPC polyclonal antibody [5 mg/ml] (SevenHills Bioreagents), mouse anti-MUC5AC monoclonal antibody [5 mg/ml] (MRQ-19, Sigma), syrian hamster anti-T1alpha (PDPN) polyclonal antibody [5 mg/ml] (Developmental Studies Hybridoma Bank), mouse anti-CLDN5 monoclonal antibody [5 mg/ml] (4C3C2, Invitrogen), rat anti-EMCN monoclonal antibody [10 mg/ml] (V.5C7, Santa Cruz), mouse anti-CGRP (human) monoclonal antibody [2 mg/ml] (Lifespan Biosciences) and rabbit anti-GRP polyclonal antibody [5 mg/ml] (Immunostar). The following secondary antibodies were used with the indicated final concentration: Cy3-conjugated goat anti-mouse IgG [2 mg/ml], Cy3-conjugated goat anti-rabbit IgG [2 mg/ml], FITC-conjugated goat anti-rabbit IgG [2 mg/ml], AF488-conjugated goat anti-rat IgG [2 mg/ml]. All images were acquired on ZEISS AxioImager 2. To quantify cells labeled by specific markers, 20X IF images were used. For each group, at least 3 mice per genotype and at least 3 sections per mouse were analyzed. Sections were selected such that they were best matching each other and covering a range of different depths.

### Immunofluorescent staining and quantification on control and NEHI lung biopsies

Immunostaining was carried out on formalin-fixed, paraffin-embedded 5-μm sections. The following antibodies were used: rabbit anti-CLDN5 monoclonal antibody (1:400; JM11-22, Invitrogen), mouse anti-CD31 monoclonal antibody (1:200; M0823, clone JC70A, Dako), rabbit anti-bombesin polyclonal antibody (1:500; ImmunoStar), and goat anti-PROX1 polyclonal antibody (1:200; R&D Systems).

For immunofluorescence staining antibodies were incubated overnight at room temperature and pretreated with citrate pH 6.0 antigen retrieval followed by endogenous biotin block. The following secondary antibodies were used: FITC and Cy3-conjugated donkey anti-rabbit IgG, FITC and Cy3-conjugated donkey anti-mouse IgG and FITC (all 1:500 from Jackson Immunoresearch). PROX1 was developed with biotinylated anti-goat antibody, streptavidin-biotin-peroxidase complex (both Vector Laboratories) and visualized with FITC TSA signal amplification system (PerkinElmer). Coverslips were mounted using Vectashield fluorescent mounting medium with DAPI (Vector Laboratories).

All slides were stained, imaged, and quantified together. For each subject, immunostaining for CLDN5 and CD31 was quantified in up to 5 random sections using the same magnification (20x), exposure time, lamp intensity and camera gain. No image processing was carried out prior to intensity analysis. CLDN5 immunostained area was expressed as a percentage of CD31 immunostained area. Images were visualized and captured with a digital camera mounted on a Nikon Eclipse 80I microscope using NIS-Elements Advanced Research Software v4.13 (Nikon Instruments Inc., Melville, NY).

### EdU analysis for cell proliferation

For EdU analysis of cell proliferation, 1 ml of 400 mM EdU solution (Thermo Scientific) was intraperitoneally injected into pregnant females. Mice were sacrificed 1 hour after EdU injection. Embryonic lungs were fixed in 4% PFA overnight and prepared for cryosectioning (10 mm). EdU was detected using the Click-iT EdU Kit with Alexa Fluor 488 (Invitrogen).

### Oxygen saturation ($SpO_2$) measurement

Pups were shaved and anesthetized by isoflurane while measurements were conducted using pulse-ox (MouseOxPlus, Starr Life Sciences). $SpO_2$ reads were recorded after 5 minutes of stable reading. Note that investigators were not, and cannot be, blinded to experimental groups during this measurement as the growth retardation of some mutant individuals was evident at this stage.

### Lung wet-to-dry ratio measurement

Individual lungs were harvested immediately after euthanasia. Excessive blood was wiped off by Kimwipe and wet weight $\mathbf{m_w}$ was measured. Lungs were then placed on foil at 70°C for 24 hours. Dry weight $\mathbf{m_d}$ was measured. Wet-to-dry ratio was calculated as: $\mathbf{W/D\ ratio=m_w/m_d}$.

### Bronchoalveolar lavage (BAL)

After sacrifice, each mouse was intratracheally injected with 1 ml saline using 1ml insulin syringe (Medline Industries). Approximately 800ul BAL was then recovered. The BAL was analyzed for for protein concentration by Pierce™ BCA Protein Assay kit (Thermo Scientific), cell counts by hemocytometer, or neuropeptide level using ELISA.

### ELISA

BAL CGRP concentration was measured by CGRP (rat) EIA Kit (Cayman Chemicals). A volume of 100ul BAL was used in each well. Final readout was performed by microplate reader (TECAN). The concentration presented is adjusted with the background detection set as 0.

Please cite this article in press as: Xu et al., Excess neuropeptides in lung signal through endothelial cells to impair gas exchange, Developmental Cell (2022), https://doi.org/10.1016/j.devcel.2022.02.023



### Tissue dissociation and sorting of single cells

After euthanasia and before tissue harvest, mice were transcardially perfused with 12 ml of cold DPBS (Life Technology). Whole lungs were mechanically dissociated in GentleMACS C tubes (Miltenyi Biotec) by running mouse lung 1-2 program on GentleMACS (Miltenyi Biotec). Lung pieces were then digested by shaking (~150 rpm) in 5 ml of PRMI 1640 (Thermo Scientific) with 10% FBS, 1mM HEPES (Life Technology), 1mM $MgCl_2$ (Life Technology), 1mM $CaCl_2$ (Sigma-Aldrich), 0.525mg/ml collagenase/dispase (Roche) and 0.25 mg DNase I (Roche) for 30 min at 37°C, followed by straining through a 70-mm filter. Red blood cells were removed by adding 1mL RBC lysis buffer (Biolegend) to each tube and incubate at room temperature for 1min.

The single-cell suspensions from above were then pelleted (1500 rpm, 4°C, 5 min), counted with hemocytometer and diluted to ~1 × $10^6$ cells per ml. They were stained with Fc blocking antibody (5 mg/ml, BD) and live/dead dye (1:2000, Ghost Dye Red 780, TONBO biosciences) at 4°C for 30 min. The cells were washed with DPBS and then incubated with surface marker antibody cocktail for 30 min at 4°C. For sorting endothelial and epithelial cells, the following antibodies were used (all antibodies were from Biolegend): 1:500 APC-conjugated anti-CD326 (G8.8); 1:500 BV510-conjugated anti-CD45 (30-F11); 1:500 PE-conjugated anti-CD31 (MEC13.3). Cell sorting was performed on a FACSAriaII high speed sorter (BD Biosciences) with four lasers (405 nm, 488 nm, 561 nm, and 640 nm). All data were further analyzed and plotted with FlowJo software (Treestar).

### Droplet-based high throughput single-cell RNA-seq and data analysis

After FACS, sorted cells were counted and processed using Chromium Single Cell 3' v3 kit (10X Genomics). Sequencing was carried out on NovaSeq (Illumina) platform at the Institute for Genomic Medicine, UCSD. Cell Ranger package (version 3.0.2) was used to align the raw reads onto the mouse reference genome (GRCm38) and generate the feature-barcode matrix. Next, R package Seurat (version 4.0) was used to perform data quality control, normalization, principal components analysis and uniform manifold approximation and projection (UMAP method). Briefly, cells with fewer than 200 or more than 2,500 unique feature counts, or more than 7% mitochondrial counts were considered low quality cells and removed from further analysis. Then global-scaling method "LogNormalize" was used to normalize the feature expression. A total of 2,000 top variable features were identified by function FindVariableFeatures and selected for subsequent principal components analysis. Top 20 significant components were chosen to conduct cell clustering by using the algorithm of uniform manifold approximation and projection (UMAP) with default settings. The expression level and feature of selected genes were profiled and visualize by R package ggplot2 (version 3.3.2).

### Western blot analysis

P22 lung tissues were collected in RIPA buffer supplemented with Complete Protease Inhibitor Cocktail tablets (Roche) and PhosSTOP Phosphatase Inhibitor Cocktail tablets (Roche). Protein samples were then homogenized in a QIAGEN TissueLyser II. Protein concentrations were measured by Pierce™ BCA Protein Assay kit (Thermo Scientific).

An estimated ~10ug protein sample was loaded in each well and ran on a 4%–12% SDS-PAGE gel (Invitrogen), followed by transfer to PVDF membranes. PVDF membranes were blocked in TBST (0.1% Tween-20) with 5% BSA for 1.5 hours, incubated in primary antibodies overnight, and then incubated in the secondary antibody for 1 hour. All imaging and quantification were performed using the Image Studio Lite software system (LI-COR Biosciences). The following primary antibodies were used: CLDN5 (Invitrogen, 4C3C2, 1:2000), CDH5 (BD, 11D4.1, 1:1500) and β-actin (Novus Biologicals, NB600501, 1:5000). The secondary antibody used were: IRDye 680RD donkey anti–mouse IgG (LI-COR, 925-69072, 1:10,000) and IRDye 680LT goat anti-rat IgG (LI-COR, 925-68029, 1:10,000). Three biological replicates were performed for each antibody.

### Evans Blue dye assay

Mice were anesthetized via IP injection of xylazine (10 mg/kg) and ketamine (100 mg/kg). Using a syringe with a 30G needle, 100 μl of 0.5 % Evans Blue in PBS was injected into the tail vein. Mice were allowed to recover on a heating pad for 1h and then sacrificed while still under anesthesia. Serum and BAL were collected as previously described (Smith et al., 2019). After BAL collection, lungs were perfused through the right ventricle with 5 ml PBS, harvested, and processed for further analysis *ex vivo*. To extract Evans Blue from lung tissue, tissues were weighed and then incubated in 250 μl formamide at 58°C for 48h.

Evans Blue in serum, lung tissue and BAL fluid was measured at 620nm by spectrophotometry. Evans Blue readings were corrected for contaminating heme in BAL fluid and lung tissue by measuring samples at 740nm and using the correction factor y = 1.193x +0.007 as previously described (Moitra et al., 2007). Lung Evans Blue level was normalized to serum Evans Blue level.

### Mouse lung angiogram

P22 mice were anesthetized via IP injection of sodium pentobarbital (120 mg/kg). After opening the chest wall, 20 IU heparin was immediately injected to the right ventricles to prevent blood coagulation. A PE-20 tube was then inserted into the main pulmonary artery via the right ventricle. 3 min pulmonary vasculature flush was performed with 37°C PBS via a syringe pump (NE-300, "Just Infusion"™) at 8.660 speed. 0.03~0.04 mL freshly prepared MicrofilVR polymer mixture (MV-122, Flow-Tech Inc.) was then gently instilled at 4.699 speed into the pulmonary vasculature until the dye reached the peripheral brunches. Lungs and hearts were then isolated and kept at 4°C overnight. Dehydration was carried out the next day after a 15 min DPBS wash with 1 hour wash in 50%, 70%, 80%, 95%, 100% and 100% ethanol solutions, respectively. To clear the lung, ethanol was replaced by 10mL/sample methyl salicylate (Sigma-Aldrich). All samples were placed on a rotator at room temperature overnight before imaging.

Please cite this article in press as: Xu et al., Excess neuropeptides in lung signal through endothelial cells to impair gas exchange, Developmental Cell (2022), https://doi.org/10.1016/j.devcel.2022.02.023





All lungs were imaged by a stereo microscope. To quantify pulmonary vasculature brunches, all brunches were outlined by Adobe Photoshop and further analyzed with ImageJ plug-in "Analyze Skeleton". Unpaired student's t test was performed for statistical analysis. More details for mouse lung angiogram analysis could be found in published literature (Xiong et al., 2021; Zhu et al., 2020).

### CGRP, BIBN-4096, and Bicuculline intranasal administration

Synthesized CGRP (Sigma-Aldrich C0292) was dissolved and diluted with saline to working concentration. A volume of 10 ul 1pg/ul CGRP was intranasally administrated to pups at P10, P12, P14 and P16. This concentration was calculated based on physiological range measured by BAL ELISA. BIBN-4096 (Fisher Scientific #45-611-0) and Bicuculline (Fisher Scientific #01-305-0) were dissolved in 100% DMSO (Sigma-Aldrich D2650) and further diluted to working solution with saline right before use. A volume of 10ul of either 0.3mg/ml BIBN-4096 or 50uM Bicuculline was intranasally administrated to pups at P10, P12, P14, P16 and P18. These concentrations were selected as previously described (Aubdool et al., 2014; Chintagari and Liu, 2012).

## QUANTIFICATION AND STATISTICAL ANALYSIS

Different quantification methods were used based on the nature of the data, as noted in individual method sections. In addition, as noted in Figure Legends, either one-way or two-way ANOVA Tukey's multiple comparisons test or Student's t test was used depending on data type. All statistical analyses were performed using Prism 6 (GraphPad).

### Quantitative PCR (qPCR)

Total RNA was extracted from lungs using Trizol (Invitrogen) and RNeasy Mini RNA extraction kit (Qiagen). RT-PCR was then performed to obtain corresponding cDNA using iScript Select cDNA Synthesis Kit (Bio-Rad). qPCR was performed by CFX Connect™ system (Bio-Rad) using SYBR Green (Bio-Rad). At least three technical and three biological replicates were performed for each gene if not otherwise notated. All primers used for qPCR analysis are listed in Table S3.

**Developmental Cell, Volume *57***

## Supplemental information

# Excess neuropeptides in lung signal through endothelial cells to impair gas exchange

**Jinhao Xu, Le Xu, Pengfei Sui, Jiyuan Chen, Esteban A. Moya, Patrick Hume, William J. Janssen, Jason M. Duran, Patricia Thistlethwaite, Aaron Carlin, Peter Gulleman, Brandon Banaschewski, Mary Kate Goldy, Jason X.-J. Yuan, Atul Malhotra, Gloria Pryhuber, Laura Crotty-Alexander, Gail Deutsch, Lisa R. Young, and Xin Sun**

# Xu et al.
# Figure S1

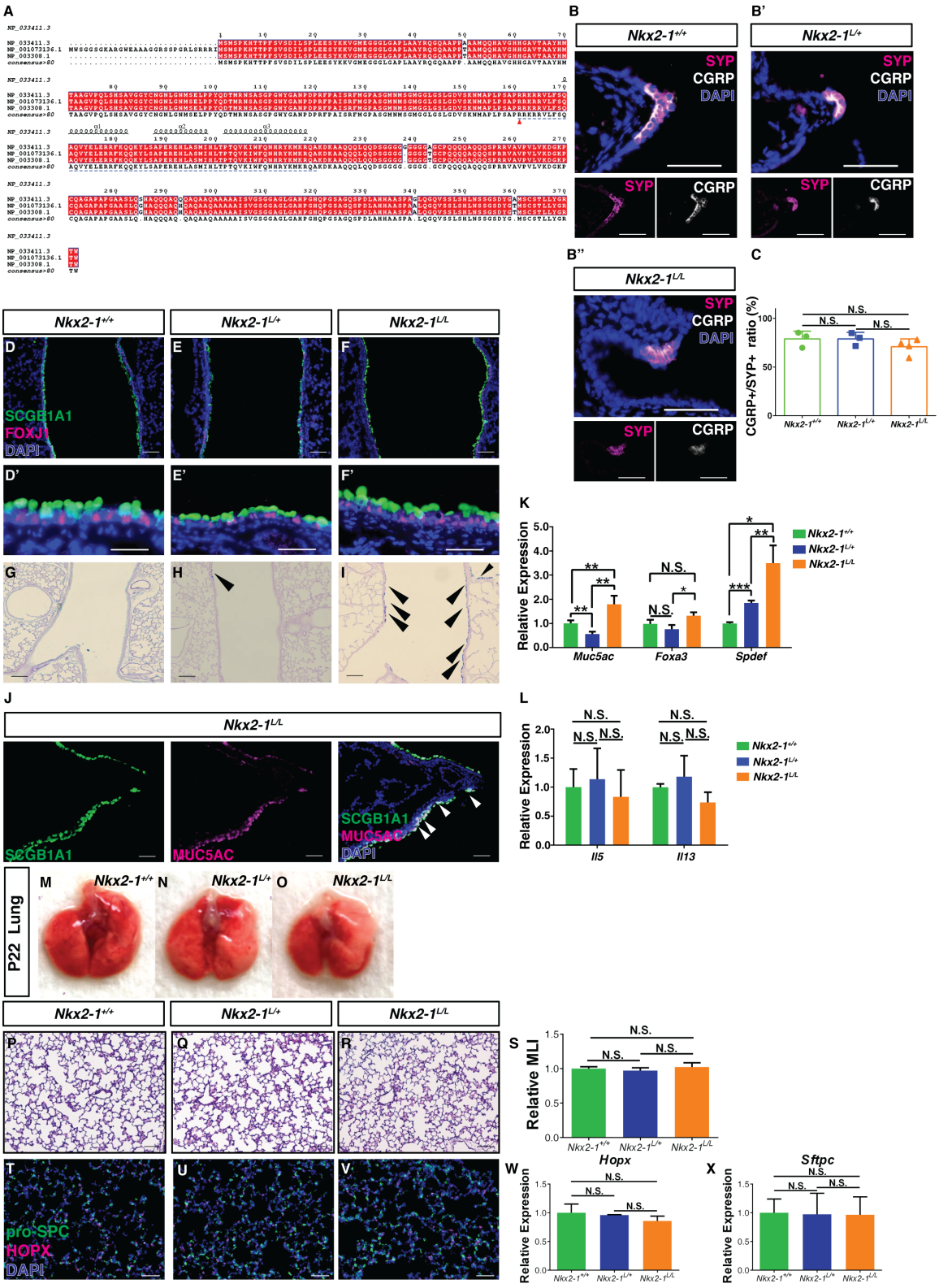

**Figure S1. *Nkx2-1*$^{L/L}$ Displays Normal Lung Size, Alveolar Architecture, Club, Ciliated, AT1, AT2 Cell Differentiation and Goblet Cell Metaplasia. Related to Figure 1.**

(A) Protein sequence alignment of mouse NKX2-1 (NP_ 033411.3), human NKX2-1 isoform 1 (NP_ 001073136.1) and human XKX2-1 isoform 2 (NP_ 003308.1). Conserved amino acids were highlighted by red. Consensus sequence was shown on the bottom. R→L point mutation position was denoted by red arrowhead. Homeobox domain was underlined by dotted line.

(B, B', B'') Representative co-staining image of SYP (magenta) and CGRP (white) labeling PNECs in P22 lung for each denoted genotype. Scale bar: 50μm.

(C) Proportion of CGRP+ PNECs as measured by the number of CGRP+ cells/ the number of SYP+ cells, each dot represents the average of an individual mouse lung across multiple sections.

(D-F) Anti-SCGB1A1 staining for club cells (green) and anti-FOXJ1 staining for ciliated cells (magenta) showed normal composition at P22. Scale bar: 100μm.

(D'-F') Magnified view of airway epithelium in respective genotypes. Scale bar: 50μm.

(G-I) PAS staining showed increased goblet cells (black arrowhead) in *Nkx2-1*$^{L/L}$ mutants at P22. Scale bar: 100μm.

(J) Anti-SCGB1A1 staining for club cells (green) and anti-MUC5AC staining for goblet cells (magenta) in *Nkx2-1*$^{L/L}$ mutant at P22. White arrowheads mark SCGB1A1+/MUC5AC+ double positive cells. Scale bar: 50μm.

(K) qPCR of goblet cell markers *Muc5ac*, *Foxa3* and *Spdef* at P22, n=3 for each group.

(L) qPCR of *Il5* and *Il13* expression at P22, n=3 for each group.

(M-O) Representative whole lung size at P22 for respective genotypes.

(P-S) H&E staining showed normal alveolar morphology at P39 in *Nkx2-1*$^{L/L}$ mutants, as quantified by mean linear intercept (MLI) analysis. Scale bar: 100μm.

(T-V) Anti-pro-SPC staining for AT2 cells (green) and anti-HOPX staining for AT1 cells (magenta) showed normal alveolar epithelial cell differentiation at P39. Scale bar: 50μm.

(W, X) qPCR of AT1 marker *Hopx* and AT2 marker *Sftpc* expression at P39 (n=3 for each group).

One-way Tukey's ANOVA multiple comparisons test was used for C, K, L, S, W, X. N.S. not significant, $p \geq 0.05$, * for $p < 0.05$, ** for $p < 0.01$, *** for $p < 0.001$. Error bars represent means ± SD.

**Xu et al.**
**Figure S2**

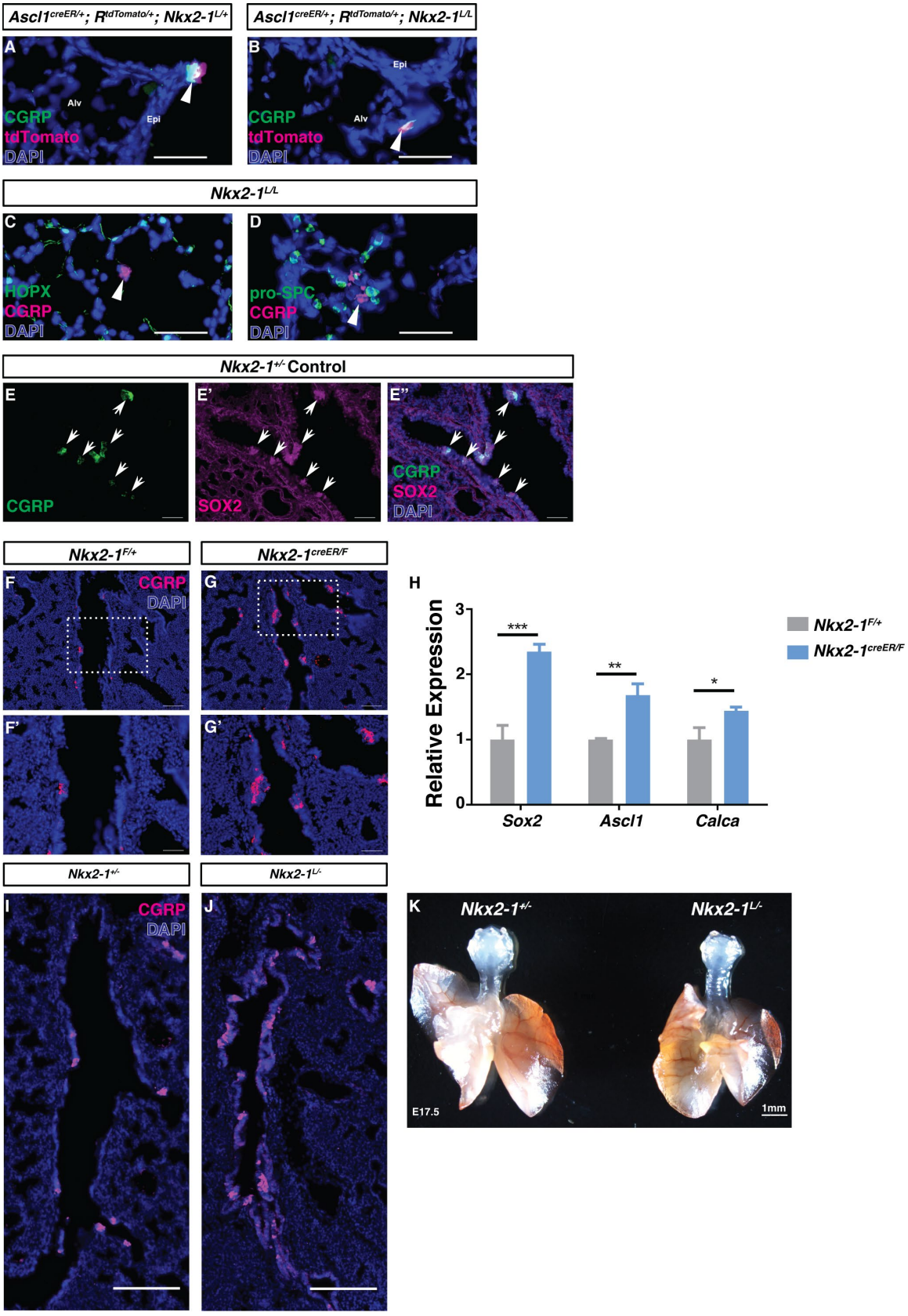

**Figure S2. *Nkx2-1*$^{L}$ Behaves as a Loss-of-function Allele. Related to Figure 2.**

(A, B) Colocalization of anti-CGRP antibody signal (green) and tdTomato signal (magenta) in airway epithelium (epi) of P14 *Nkx2-1*$^{L/+}$ control and alveolar region (alv) of *Nkx2-1*$^{L/L}$ mutant with *Ascl1-creER; Rosa-tdTomato* lineage tracing, respectively. CRE activation was triggered by tamoxifen injection to pregnant females at E13.5.

(C, D) Anti-CGRP staining of ectopic PNECs in the alveolar region (magenta, arrowheads) showed no colocalization with AT1 marker anti-HOPX staining (C, green) or AT2 marker anti-pro-SPC staining (D, green). Scale bar: 50μm.

(E-E'') Anti-CGRP staining (green) and anti-SOX2 staining (magenta) showed colocalization of PNECs and relatively higher SOX2 intensity. Scale bar: 50μm

(F, G) Representative E17.5 main airway with anti-CGRP staining showing increased PNECs in partial loss-of-function mutant *Nkx2-1*$^{creER/F}$ compared to control. Inactivation was triggered by tamoxifen injection of pregnant females at E13.5. Scale bar: 100μm.

(F', G') Magnified view of boxed areas in A and B, respectively. Scale bar: 50μm.

(H) qPCR of *Sox2*, *Ascl1* and *Calca* expression of E17.5 lung. Student's *t* test was used. * for $p<0.05$, ** for $p<0.01$, *** for $p<0.001$. Error bars represent means ± SD.

(I, J) Representative E17.5 main airways with anti-CGRP staining marking PNECs. Scale bar: 100μm.

(K) Representative lung size comparison between littermates at E17.5.

**Xu et al.**
**Figure S3**

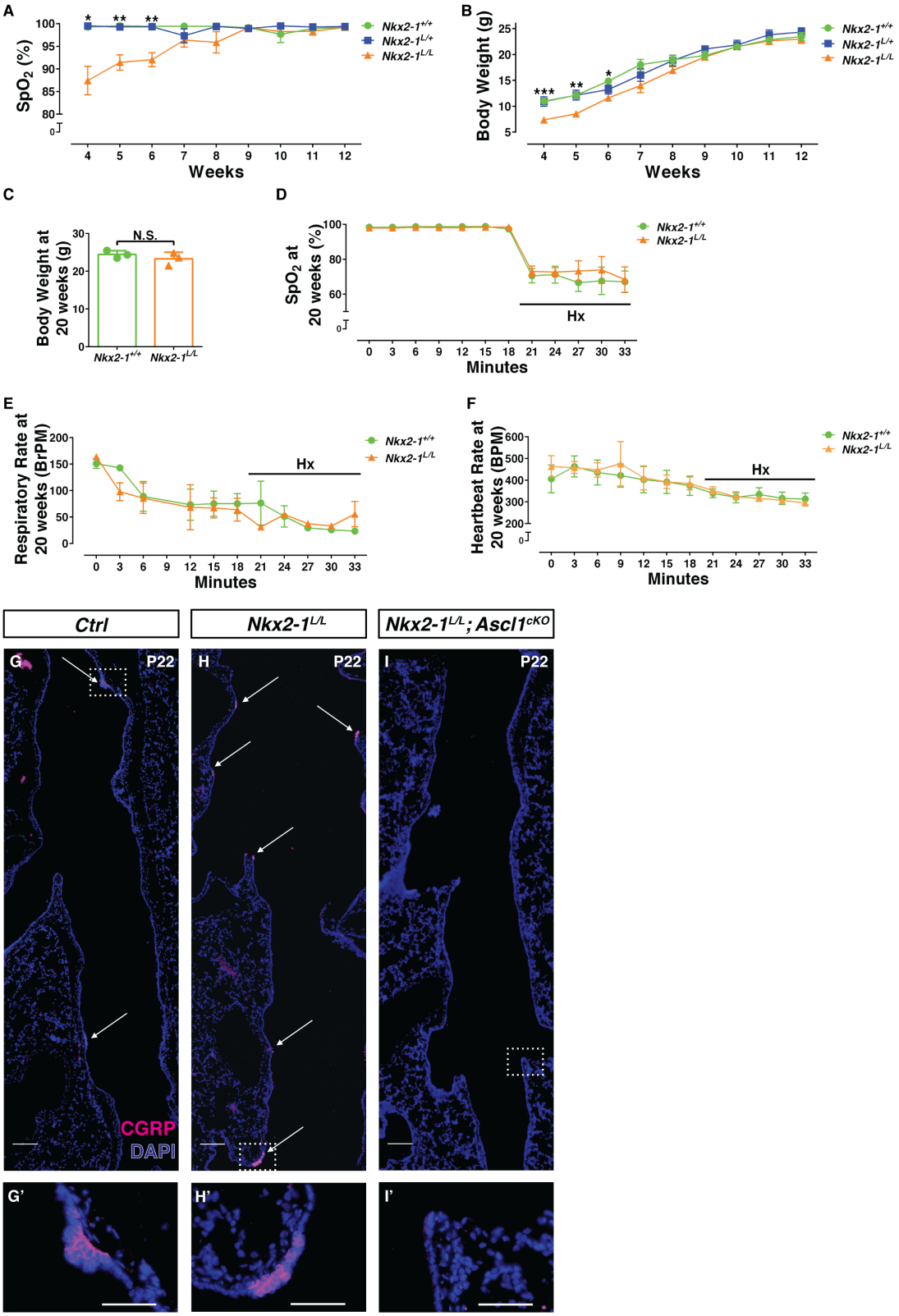

**Figure S3. NEHI-like Phenotypes Improve with Age in *Nkx2-1*$^{L/L}$ Mutants. Related to Figure 3.**

(A, B) Growth curve (A) and oxygen saturation (B) as measured each week from Week 4 to Week 12 after birth of 9 individuals (n=3 for each group, all females). One-way ANOVA Tukey's multiple comparisons test was used at each time point. * for $p<0.05$, ** for $p<0.01$, *** for $p<0.001$. Error bars represent means ± SEM.

(C) Body weight comparison at 20 weeks (n=3 for each group, all females). Student's *t* test was used. N.S. not significant, $p\geq0.05$. Error bars represent means ± SEM.

(D-F) Oxygen saturation (D), respiratory rate (E) and heartbeat rate (F) was measured in 3-min intervals under normoxia (21% $O_2$, 0-20 min) or hypoxia (7% $O_2$, 20-35min) conditions on 20-week-old individuals (n=3 for each group, all females). One-way ANOVA Tukey's multiple comparisons test was used at each time point, no significant difference was detected. Error bars represent means ± SEM. Hx, hypoxia. BrPM, breaths per minute. BPM, beats per minute.

(G-I) Representative longitudinal sections of the main airway in P22 lungs of *Ctrl* (*Nkx2-1*$^{L/+}$*; Shh*$^{cre}$*; Ascl1*$^{F/+}$, G) *Nkx2-1*$^{L/L}$ (*Nkx2-1*$^{L/L}$*; Shh*$^{cre}$*; Ascl1*$^{F/+}$, H) and *Nkx2-1*$^{L/L}$*; Ascl1*$^{cKO}$ (*Nkx2-1*$^{L/F}$*; Shh*$^{cre}$*; Ascl1*$^{F/F}$, I) genotypes, respectively. Anti-CGRP staining marked PNECs (arrows). Scale bar: 100μm.

(G'-I') Magnified view of boxed areas in A-C, correspondingly. Scale bar: 50μm.

**Xu et al.**
**Figure S4**

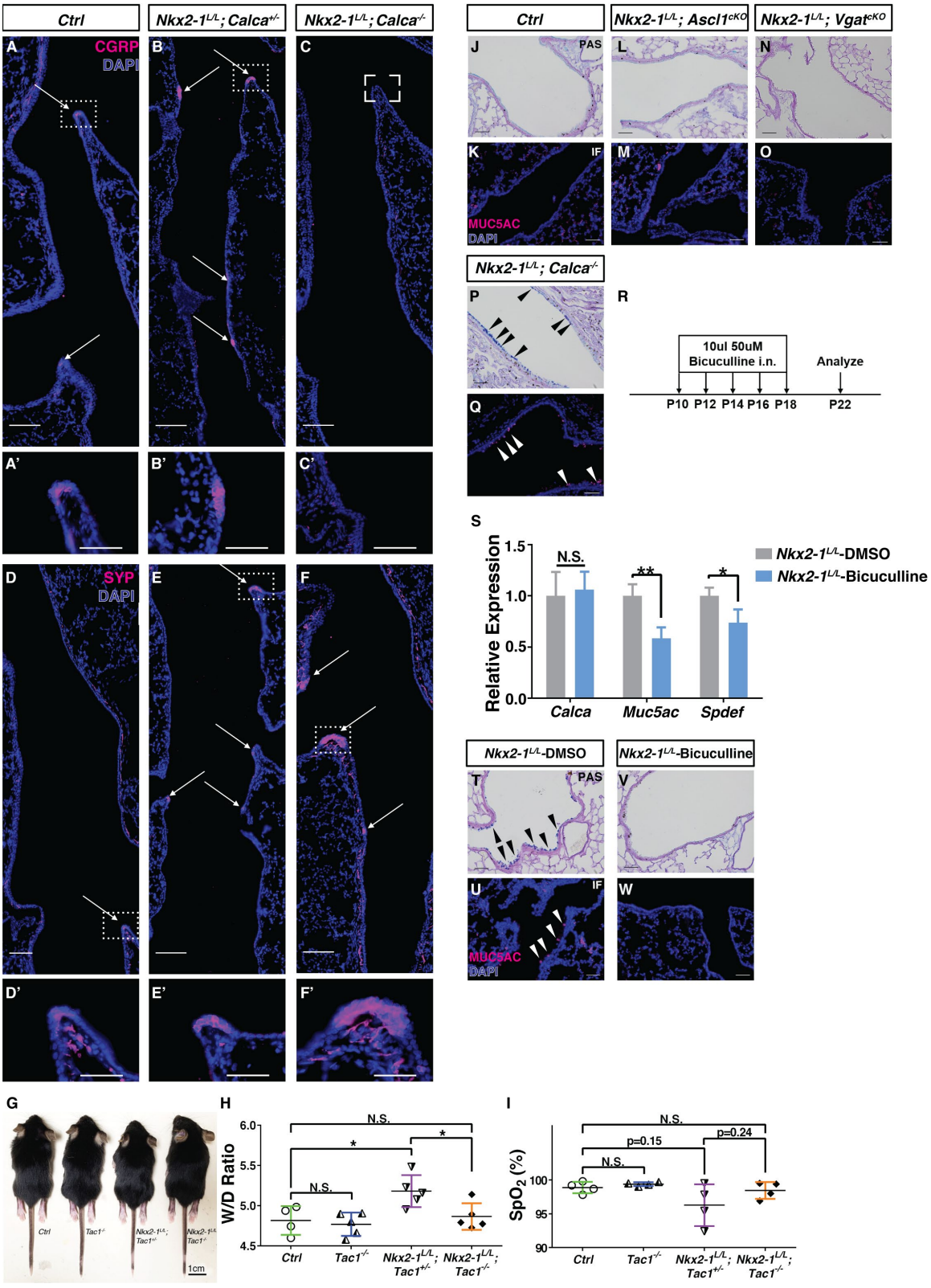

**Figure S4. Genetic or Pharmacological Inhibition of PNEC Products Attenuated Defects in *Nkx2-1$^{L/L}$* Mutants. Related to Figure 4.**

(A-C) Representative longitudinal sections of the main airway in P22 lungs of *Ctrl* (*Nkx2-1$^{L/+}$; Calca$^{+/-}$*), *Nkx2-1$^{L/L}$; Calca$^{+/-}$* and *Nkx2-1$^{L/L}$; Calca$^{-/-}$* genotypes, respectively. Arrows indicate anti-CGRP staining signal. Scale bar: 100μm.

(A'-C') Magnified boxed areas in A-C, respectively. Scale bar: 50μm.

(D-F) Representative longitudinal sections of the main airway in P22 lungs of *Ctrl* (*Nkx2-1$^{L/+}$; Calca$^{+/-}$*), *Nkx2-1$^{L/L}$; Calca$^{+/-}$* and *Nkx2-1$^{L/L}$; Calca$^{-/-}$* genotypes, respectively. Anti-SYP staining marks PNECs (arrows) and nerve fibers. Scale bar: 100μm.

(D'-F') Magnified view of boxed areas in A-C, respectively. Scale bar: 50μm.

(G) Representative body size at P22 for each group.

(H) Lung W/D ratio for each group (n≥4 for each group) Student's *t* test. N.S. not significant, p≥0.05. * for p<0.05. Error bars represent means ± SD.

(I) Oxygen saturation at P22 (n=4 for each group). Note that while *Nkx2-1$^{L/L}$; Tac1$^{-/-}$* mutants showed improved oxygen saturation back to baseline level, compared to *Nkx2-1$^{L/L}$; Tac1$^{+/-}$* mice, this change did not reach statistical significance partially due to a large variation of measurements in the *Nkx2-1$^{L/L}$; Tac1$^{+/-}$* mice. Two-way ANOVA Tukey's multiple comparisons test was used. N.S. not significant, p≥0.05. * for p<0.05. Error bars represent means ± SD.

(J-Q) PAS staining and anti-MUC5AC staining (magenta) labeled goblet cells in the distal airway of indicated genotypes. *Nkx2-1$^{L/L}$*; *Ascl1$^{cKO}$* and *Nkx2-1$^{L/L}$*; *Vgat$^{cKO}$* airways exhibited no goblet cell metaplasia, similar to *Ctrl* (*Nkx2-1$^{L/+}$*). In contrast, *Nkx2-1$^{L/L}$*; *Calca$^{-/-}$* airway continued to exhibit increased goblet cells. Scale bar: 50μm.

(R) Regimen of intranasal Bicuculline administration. Dose was selected based on published literature (Chintagari and Liu, 2012).

(S) qPCR of PNEC marker *Calca* and goblet cell markers *Muc5ac* and *Spdef* at P22, n=3 for each group. Student's *t* test was used. N.S. not significant, p≥0.05. * for p<0.05, ** for p<0.01. Error bars represent means ± SD.

(I-W) PAS staining, and anti-MUC5AC staining (magenta) showed absence of goblet cell signal in Bicuculline-treated *Nkx2-1$^{L/L}$* mutants compared to DMSO-treated vesicle control group.

**Xu et al.**
**Figure S5**

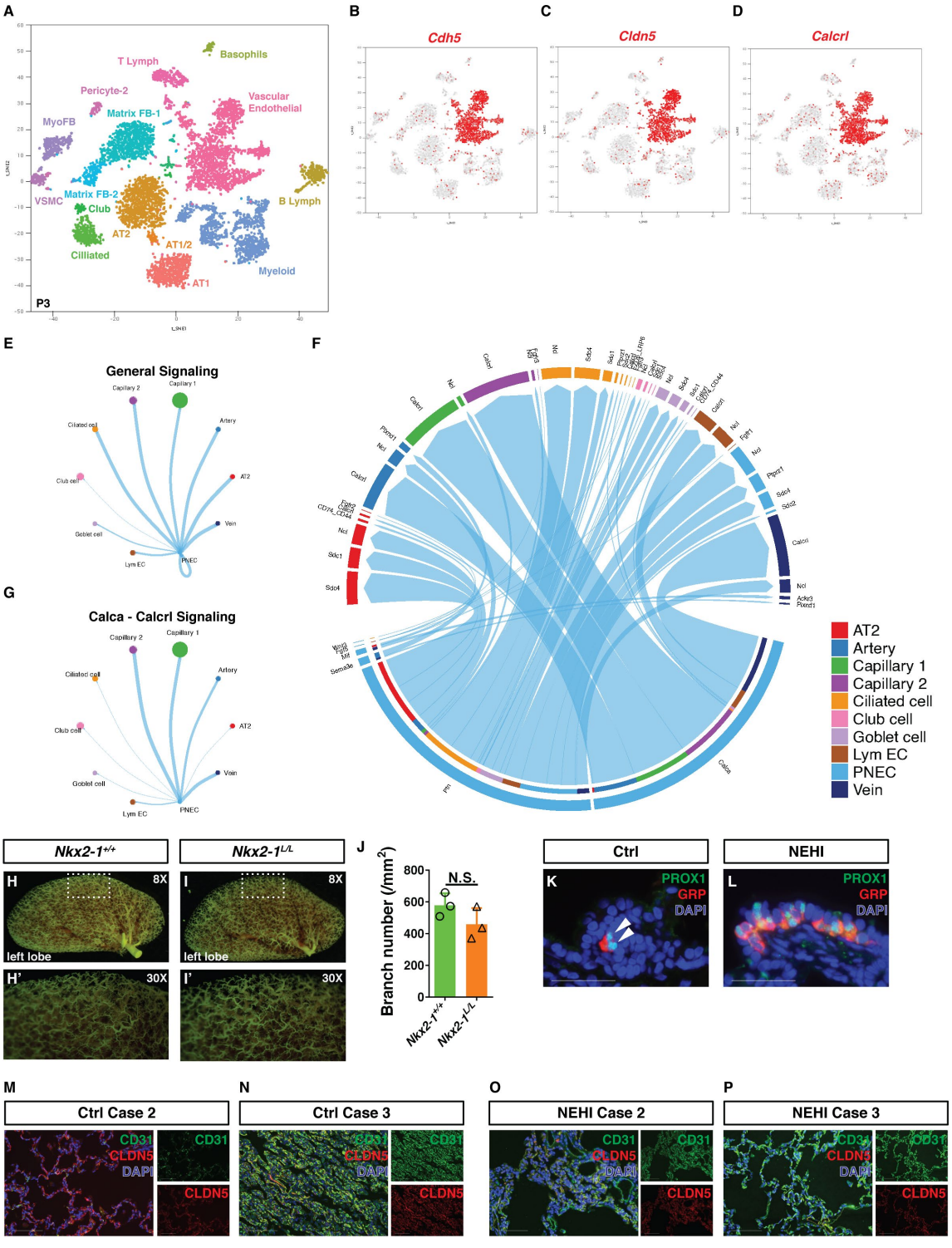

**Figure S5. Endothelial Cells are the Primary Target Cell Type of CGRP. Related to Figure 5.**

(A) LungMAP t-distributed stochastic neighbor embedding (t-SNE) plot of major cell populations annotated in scRNA-seq data of P3 mouse lung (Du et al., 2017).

(B-D) LungMAP t-SNE patterns of *Cdh5* (pan-endothelial marker); (B) *Cldn5*; (C) and *Calcrl* (D) denoted by red dots. Panels were downloaded from LungGENS website.

(E-G) Cell-cell interaction analysis of our P3 mouse lung (both control and mutant lungs integrated) single cell data using CellChat (Jin et al., 2021). Overall signaling (E), detailed signaling pathways (F) and CALCRL-CGRP interaction (G) between PNECs and endothelial cells are shown in circuit plots. The width of each line indicates signaling strength while arrows point to receiver cells. In F, each secretory ligand and its receptor were labeled.

(H, I) Representative angiogram of whole lung lobes from *Nkx2-1*$^{+/+}$ and *Nkx2-1*$^{L/L}$ mice at P22 that did not shown leakage, magnification: 8X.

(H', I') Magnified boxed areas in H and I, respectively. Magnification: 30X.

(J) Quantifications of endothelial branch numbers per area for left lobes from *Nkx2-1*$^{+/+}$ and *Nkx2-1*$^{L/L}$ mice at P22. N=3 for each group. Student's *t* test was used. N.S. not significant. Error bars represent means ± SD.

(K, L) Representative anti-PROX1 antibody (green) and anti-GRP antibody double staining (red) showed an increase of PNEC specification marker PROX1 in NEHI biopsies (K) compared to normal lung biopsies (L). Scale bar: 50μm.

(M-P) Anti-CD31 antibody (green) and anti-CLDN5 antibody double staining (red) showed a trending decrease of CLDN5 in NEHI biopsies (O, P) compared to normal lung biopsies (M, N), representative of multiple sections assayed from individual donors in addition to those in Figure 5T and 5U. Scale bar: 100μm.

**Xu et al.**
**Figure S6**

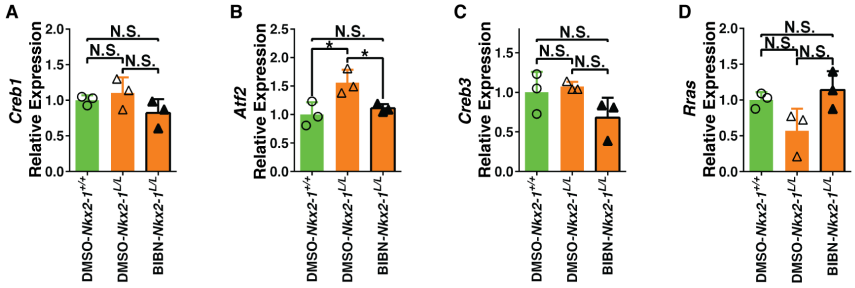

**Figure S6. cAMP Signaling was Reversed upon BIBN Treatment in *Nkx2-1*$^{L/L}$ Mutants. Related to Figure 6.**

(A-D) qPCR of cAMP signaling gene *Creb1*, *Atf2* (*Creb2*), *Creb3*, and *Rras* at P22, n=3 for each group. One-way ANOVA Tukey's multiple comparisons test was used. N.S. not significant. * for $p < 0.05$. Error bars represent means ± SD.

**Table S1. NEHI and control cohort metadata. Related to Figure 5.**

| Sample No. | Diagnosis | Age | Sex |
|---|---|---|---|
| #1 | NEHI | 5 weeks | Male |
| #2 | Mild deficient alveolarization and PH | 5 weeks | Male |
| #3 | NEHI | 3 months | Female |
| #4 | Normal lung (lobectomy for focal | 5 months | Female |
| #5 | NEHI | 6 months | Female |
| #6 | Chronic bronchiolitis (Aspiration) | 7 months | Male |
| #7 | NEHI | 20 months | Female |
| #8 | Normal lung (lobectomy for focal | 2 years | Female |

**Table S2. Human adult lung tissue donor metadata. Related to Figure 7.**

| Sample No. | Sample Type | Donor ID | Age | Sex |
|---|---|---|---|---|
| #1 | control-surgical | HL2 | 58 | Male |
| #2 | control-surgical | HL3 | 72 | Male |
| #3 | control-surgical | HL4 | 76 | Male |
| #4 | control-surgical | HL5 | 46 | Female |
| #5 | control-autopsy | D231 | 33 | Female |
| #6 | control-autopsy | D239 | 37 | Male |
| #7 | control-autopsy | D271 | 53 | Male |
| #8 | control-autopsy | CO488 | 25 | Male |
| #9 | COVID ARDS | COVID 0501 | 88 | Female |
| #10 | COVID ARDS | COVID 0601 | 57 | Male |
| #11 | COVID ARDS | COVID 0611-2 | 65 | Male |
| #12 | COVID ARDS | COVID 0522 | 65 | Male |
| #13 | COVID ARDS | COVID 0722 | 67 | Male |
| #14 | COVID ARDS | D269 | 85 | Male |
| #15 | COVID ARDS | D274 | 70 | Male |
| #16 | non-COVID | CO441 | 39 | Female |
| #17 | non-COVID | CO446 | 23 | Male |
| #18 | non-COVID | CO447 | 61 | Female |

**Table S3. qPCR primer list. Related to STAR Methods.**

| Gene name | Sequence |
|---|---|
| *Actb(β-actin)* | 5′-CGGCCAGGTCATCACTATTGGCAAC-3′<br>5′-GCCACAGGATTCCATACCCAAGAAG-3′ |
| *Ascl1* | 5′-TCTGGCAAGATGGAGAGTGGAGC-3′<br>5′-AAAGAAGCAGGCTGCGGGAG-3′ |
| *Atf2* | 5′-GAGGAGCCTTCTGTTGTAGAAAC-3′<br>5′-GACGAACGATAGCTGATGTGG-3′ |
| *Calca* | 5′-CCTTTCCTGGTTGTCAGCATCTTG-3′<br>5′-CTGGGCTGCTTTCCAAGATTGAC-3′ |
| *Cldn5* | 5′-ACGGGAGGAGCGCTTTAC-3′<br>5′-GTTGGCGAACCAGCAGAG-3′ |
| *Creb1* | 5′-AGCAGCTCATGCAACATCATC-3′<br>5′-AGTCCTTACAGGAAGACTGAACT-3′ |
| *Creb3* | 5′-ACAGGAGCACGTCTCCATAGA-3′<br>5′-CGGTCAGTATCAGCCTAGACAT-3′ |
| *Foxa3* | 5′-CTTGGTGGAGGTTGGGTGAG-3′<br>5′-ACAGGCAGTATTCCCAAGCC-3′ |
| *Hes1* | 5’-TGCCAGCTGATATAATGGAGAA-3’<br>5’-CCATGATAGGCTTTGATGACTTT-3’ |
| *Hopx* | 5’-CCACGCTGTGCCTCATCGCA-3’<br>5’-GGCCTGGCTCCCTAGTCCGT-3’ |
| *Il5* | 5′-CCTCTTCGTTGCATCAGGGT-3′<br>5′-GATCCTCCTGCGTCCATCTG-3′ |
| *Il13* | 5′-AAAGCAACTGTTTCGCCACG-3′<br>5′-CCTCTCCCCAGCAAAGTCTG-3′ |
| *Muc5ac* | 5′-TGACTCAATCTGCGTGCCTT-3′<br>5′-AGGCCTTCTTTTGGCAGGTT-3′ |
| *Notch1* | 5’-CTCCGTTACATGCAGCAGTT-3’<br>5’-CCAGGATCAGTGGAGTTGTG-3’ |

| | |
|---|---|
| *Notch2* | 5’-TGCCTGTTTGACAACTTTGAGT-3’<br>5’-GTGGTCTGCACAGTATTTGTCAT-3’ |
| *Sftpc* | 5’-ATGGACATGAGTAGCAAAGAGGT-3’<br>5’-CACGATGAGAAGGCGTTTGAG-3’ |
| *Sox2* | 5’-TAGAGCTAGACTCCGGGCGATGA-3’<br>5’-TTGCCTTAAACAAGACCACGAAA-3’ |
| *Spdef* | 5′-GACTGTGGAATTCCTGGGGG-3′<br>5′-ATTGTGGCAGGAGCAGAGAC-3′ |